Bridgeless Cuk-Derived Single Power Conversion Inverter With Reactive-Power Capability

Byeongcheol Han, *Member, IEEE*, Jih-Sheng Lai, *Life Fellow, IEEE*, and Minsung Kim, *Member, IEEE*

***Abstract*—This paper presents a bridgeless Cuk-derived single power conversion inverter with reduced number of power components, which has reactive-power capability. The secondary diode of the conventional unfolding-type Cuk inverter is integrated into one of the secondary-side switches in the bridgeless Cuk-derived configuration, which reduces the number of active-power components. A modulation technique is developed to provide a current path during reverse power flow; this technique enables operations under unity and nonunity power factors. A repetitive controller coupled with a linear feedback controller and a feed-forward controller are used to achieve accurate output current tracking under the harsh control environment. Driving the diode-integrated switch in synchronous rectification mode provides higher power conversion efficiency than that under diode-based secondary side rectification. Circuit operation and design guidelines of the bridgeless Cuk inverter are presented in detail. A 500-VA prototype inverter was fabricated to demonstrate the desirable performance of the bridgeless Cuk-derived inverter.**

***Index Terms*—Cuk topology, modulation technique, reactive-power injection, reduced number of power components, synchronous rectification (SR).**

I. INTRODUCTION

IN RECENT years, small-scale, decentralized grid-connected renewable energy systems have shown the potential to meet the demand for clean and reliable electricity while mitigating global warming and environmental pollution. In renewable energy systems, module-integrated converters (MICs) capture electric power from each energy module and supply it to the utility grid. MICs among photovoltaic (PV) inverters are easy to install and maintain, eliminate high-voltage dc wiring, and they have high power yield under partial shading [1]. MICs will dominate the residential PV market in a few years [2].

An important issue of grid-connected inverters is their ability to supply reactive power into the utility grid. Nowadays, some regulations such as VDE-AR-N4105 [3] require that a definite amount of reactive power should be processed by grid-connected inverters that have medium- and high-power levels for renewable energy systems. As the market share of MICs increases, similar regulations will be enacted to impose reactive-power-transfer capability on inverters that have low power level, including MICs.

A two-stage conversion approach [4]–[6] is straightforward and can be used in single-phase MICs. It consists of a step-up dc–dc converter, which boosts the low voltage of energy sources to the dc-link compatible voltage, while tracking the maximum power point (MPP), and a dc–ac inverter transferring the energy stored in the dc-link capacitor to the utility grid. At the step-up stage, a hybrid-mode series resonant converter has been developed in [4]. By utilizing a bidirectional ac switch, it operates in phase-shift series resonant converter when the input voltage is higher than the nominal input voltage; it operates in resonant boost converter when the input voltage is lower than the nominal input voltage. Thus, it achieves high efficiency over a wide input voltage range. A dual-active-bridge converter can be used at dc–dc converter stage. Since it suffers from poor efficiency at low power, Poshtkouhi and Trescases [5] presented the flyback mode operation of a dual-active-bridge converter, which improves power conversion efficiency at low power. A dual-series resonant converter has also been used at front-end converter stage. It features a small number of power components, inherent boosting ability, and high efficiency [6]. At the dc–ac inverter stage, the H-bridge inverter with a bipolar pulsewidth modulation (PWM) technique [8] has been widely used. It shows relatively low efficiency compared to that of the H-bridge inverter with a unipolar PWM, but it can inject reactive power into the utility grid at any desired power factor. Since then, to satisfy international safety standards for leakage current, modified H-bridge topologies such as H5, H6, and highly efficient and reliable inverter concept (HERIC) inverters have been suggested. These inverters can eliminate the leakage current that exists in transformerless inverters. However, traditional modulation techniques for these inverters cannot generate the reactive current. Recently, new modulation techniques for H5 inverters [9], H6 inverters [10], [11], and HERIC inverters [12] have been actively researched, which enable these inverters to inject reactive current into the grid. However, these two-stage conversion approaches require many power components, which results in low efficiency and high cost; these aspects are not desirable in low power level inverters.

As an alternative to the two-stage conversion approach, a single-stage conversion approach has been presented and

---

Manuscript received November 7, 2018; revised February 25, 2019 and May 6, 2019; accepted July 2, 2019. Date of publication July 8, 2019; date of current version December 13, 2019. This work was supported by the Basic Science Research Program through the National Research Foundation of Korea funded by the Ministry of Education under Grant 2018R1D1A1B07044999. Recommended for publication by Associate Editor M. Amirabadi. *(Corresponding author: Minsung Kim.)*

B. Han and J.-S. Lai are with the Future Energy Electronics Center, Virginia Polytechnic Institute and State University (Virginia Tech), Blacksburg, VA 24061 USA (e-mail: hbychol@vt.edu; laijs@vt.edu).

M. Kim is with the Division of Electronics and Electrical Engineering, Dongguk University, Seoul 04620, South Korea (e-mail: mkim@dongguk.edu).

Color versions of one or more of the figures in this paper are available online at http://ieeexplore.ieee.org.

Digital Object Identifier 10.1109/TPEL.2019.2927645

adopted in MICs. It converts the low voltage of energy sources into a high-voltage ac signal in a single step. Therefore, it provides higher power conversion efficiency and lower cost than those provided by the two-stage conversion approach. Among the many topologies applicable to the MIC technology, unfolding-type flyback inverters [13], [14] have been widely used because they feature simple structure, low component number, and high efficiency. Very recently, the output power of MICs has been progressively pushed to higher levels, and this change imposes new operational and structural challenges for the conventional unfolding-type flyback inverters. Favorable schemes that can broaden the power level include adopting an interleaving technique [15] or adding an adaptive snubber [16] or an active-clamp circuit [17] to the conventional flyback inverters; a flyback inverters operating in continuous conduction mode (CCM) [18]–[20] has also been proposed. Despite these efforts, the operating power range of unfolding-type flyback inverters is limited to 300 W due to the low transformer utilization factor. To further increase the power level, unfolding-type Cuk inverters operating in CCM [21] and hybrid mode [22] have been proposed for MICs. Unfolding-type Cuk inverters feature wide input voltage range, galvanic isolation, and low ripples of input current and output current. In addition, their magnetizing current in the transformer can be available in both directions; this trait increases the utilization of the transformer and, therefore, increases power capacity [23].

However, the above unfolding-type inverters (e.g., unfolding-type flyback/Cuk inverters) cannot supply reactive power into the grid because they lack a current path in the unfolding circuit and, as a result, show severe current distortion around the zero-voltage crossing [24]. By modifying the reference output current to a quasi-sinusoidal waveform [25], reactive power can be carried without having to use any additional circuit, but this approach increases total harmonic distortion (THD) to an unacceptable level. Additional control circuits such as static synchronous compensator (STATCOM) [26], active-power filtering [27], or decoupling circuit [24] can help the unfolding-type inverter generate reactive current. The STATCOM consists of a voltage source converter and a grid-connecting inductor; this circuit is used for static reactive-power compensation [26]. The active-power filter along with adaptive dc-link voltage controller has been presented in [27]. It achieves dynamic reactive-power compensation while reducing the switching loss and noise. A current decoupling circuit [24] has been connected at the grid side of the unfolding-type flyback inverter; it has been used to alleviate the current distortion problem around the zero-voltage crossing when the reference output current is phase-shifted. However, all of these additional circuits increase the hardware implementation cost. A differential-mode Cuk inverter, one of the Cuk-derived topologies, has been developed for single-phase and three-phase utility grids [28], [29]. This inverter can transfer the reactive power to the grid. The differential-mode Cuk inverter is composed of multiple modules, which are connected in parallel at the dc side and connected in series at the ac side. This architecture leads to having a large number of power components.

This paper presents a bridgeless Cuk-derived single power conversion inverter with reactive-power capability. It features simple structure and has low cost because it does not have a secondary-side diode; its function is conducted by one of the two switches on the secondary side depending on the polarity of the grid voltage. To achieve active-/reactive-power injection, this paper also presents the modulation scheme for the bridgeless Cuk-derived inverter topology. A repetitive controller (RC) coupled with a linear feedback controller and a feed-forward controller is used to obtain accurate tracking of the reference output current. Furthermore, the power conversion efficiency is improved significantly when the diode-integrated switch operates in synchronous rectification (SR) mode. The design guidelines of the bridgeless Cuk-derived inverter are presented, and the experimental results are obtained using a 500-VA prototype inverter.

This paper is organized as follows. The bridgeless Cuk-derived inverter is described in Section II, and a control design for the inverter is proposed in Section III. The design guidelines are given in Section IV, and the experimental results are presented and the methods for reactive-power support are compared in Section V. The conclusion is drawn in Section VI.

II. BRIDGELESS CUK-DERIVED SINGLE POWER CONVERSION INVERTER

The bridgeless Cuk-derived inverter [see Fig. 1(a)] consists of inductors L_1, L_2; primary-side switch S_1 and its body-diode D_{S_1}; capacitors C_1, C_2, C_3; ideal transformer T with turns ratio $n = N_s/N_p$; secondary-side switches S_2–S_5 and their body diodes D_{S_2}–D_{S_5}; output filter inductor L_f. Furthermore, v_{in} is dc input voltage and v_g the ac-grid voltage. At the primary side of the transformer, the inverter comes with a boost converter, where a node of its output capacitor is connected to the upper node of the transformer. At the secondary side of the transformer, it employs four switches S_2–S_5. For operation under unity power factor, switch S_4 or S_5 works as the secondary-side diode of the conventional Cuk converter. Meanwhile, other switch pairs (S_2 and S_5, or S_3 and S_4) serve as the unfolding-bridge circuit. For operation under nonunity power factor, the switching operation is the same as the operation under unity power factor when the power flow is forward, but when the power flow is reversed, switches S_4 or S_5 operate at high frequency instead of S_1.

Table I summarizes the comparison of Cuk-topology-based inverters. The bridgeless Cuk-derived inverter [see Fig. 1(a)] is a modification of the topology in [36], and it does not require the additional secondary-side diode that the unfolding-type Cuk inverter uses [see Fig. 1(b)]. Also, the proposed inverter can transfer reactive power to the utility grid owing to the high-frequency operation of the secondary-side switches for the reversed power flow. The differential-mode Cuk inverter [see Fig. 1(c)] requires fewer active-power components, but it also requires many more passive-power components than required by the bridgeless Cuk-derived inverter.

A. Operation Principles

The operation of the bridgeless Cuk-derived inverter is classified according to the direction of power flow. Power is transferred from the input side to the grid during forward power flow, and from the grid to the input side during reverse power flow. Accordingly, the operation can be divided into four sectors according to the grid-current direction and the grid-voltage polarity (see

TABLE I
COMPARISON OF CUK-DERIVED INVERTERS FOR MIC APPLICATIONS

Cuk topology-based inverters	# of components					High-frequency switching components	Reactive power capability	Ref.
	S	D	L	C	T			
Unfolding-type Cuk inverter	5	1	2	3	1	2	No	[21, 22]
Differential-mode Cuk inverter	4	0	4	6	2	2	Yes	[28]
Bridgeless Cuk-derived inverter	5	0	2	3	1	2	Yes	-

S: switch, D: diode, L: inductor, C: capacitor, T: transformer.

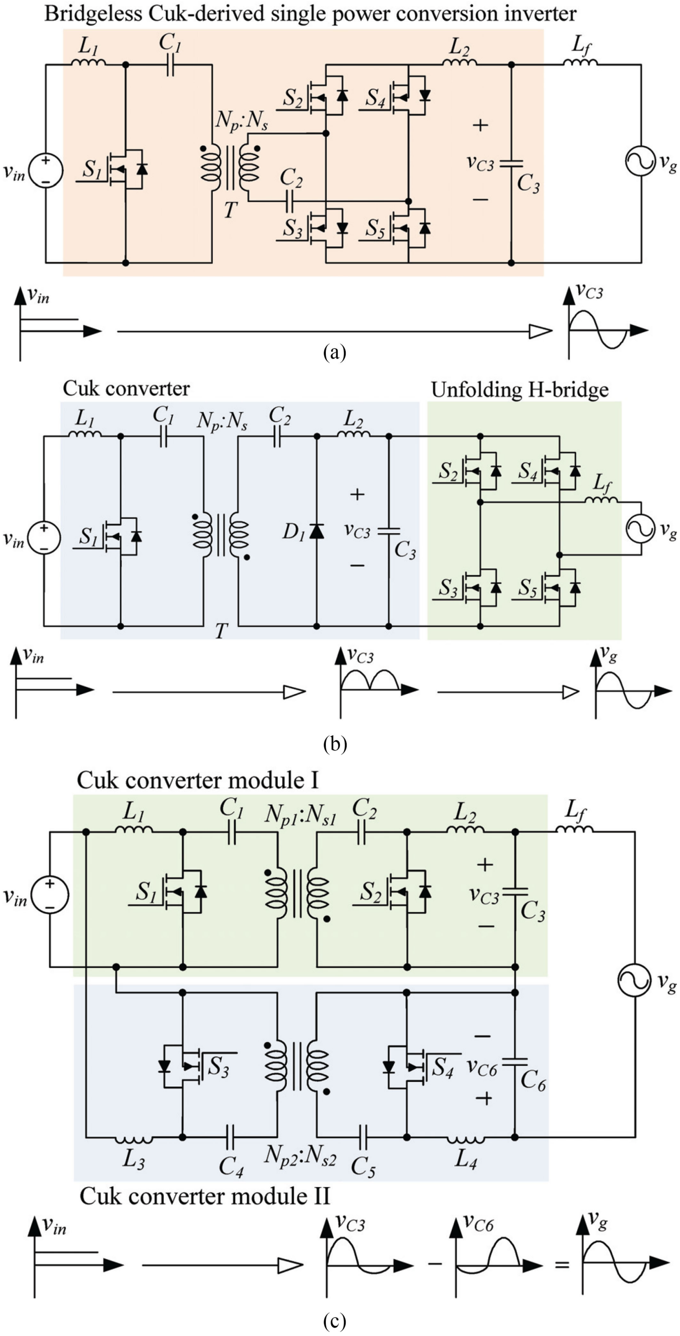

Fig. 1. Circuit diagrams of the Cuk-topology-based inverters. (a) Proposed bridgeless Cuk-derived single power conversion inverter. (b) Unfolding-type Cuk inverter. (c) Differential-mode Cuk inverter.

TABLE II
OPERATING SECTORS OF BRIDGELESS CUK-DERIVED INVERTER

		Voltage polarity	
		Positive ($v_g > 0$)	Negative ($v_g < 0$)
Current direction	Forward ($i_o > 0$)	I (forward power flow)	II (reverse power flow)
	Backward ($i_o < 0$)	III (reverse power flow)	IV (forward power flow)

v_g: grid voltage, i_o: output current.

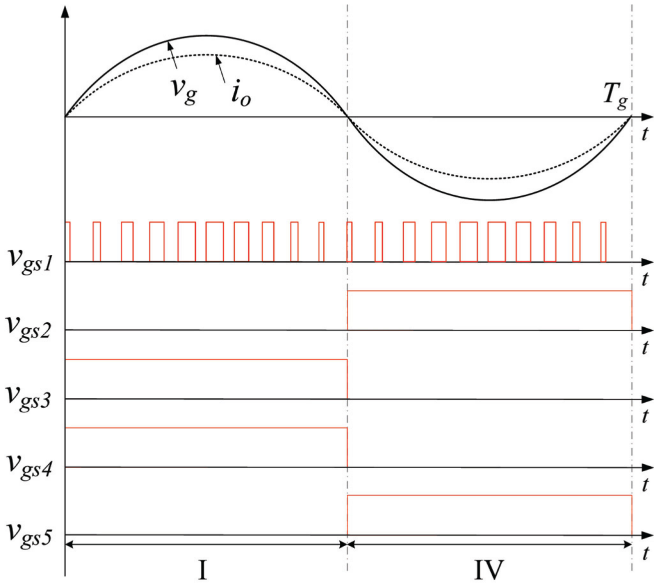

Fig. 2. Waveforms of gate drive signals for unity power factor operation.

Table II). This bidirectional power-flow characteristic enables the bridgeless Cuk-derived inverter to supply both active power and reactive power into the grid.

The operation principles are based on the assumption that the inductances of L_1 and L_2 are sufficiently large to make the inverter operate in the CCM; the capacitance of C_1 is also large enough such that the voltage across C_1 is considered as a constant in a switching period and the steady-state voltage across C_1 is equal to the input voltage v_{in}.

1) Unity Power Factor: During the operation under unity power factor (see Fig. 2), the grid current flows in the same

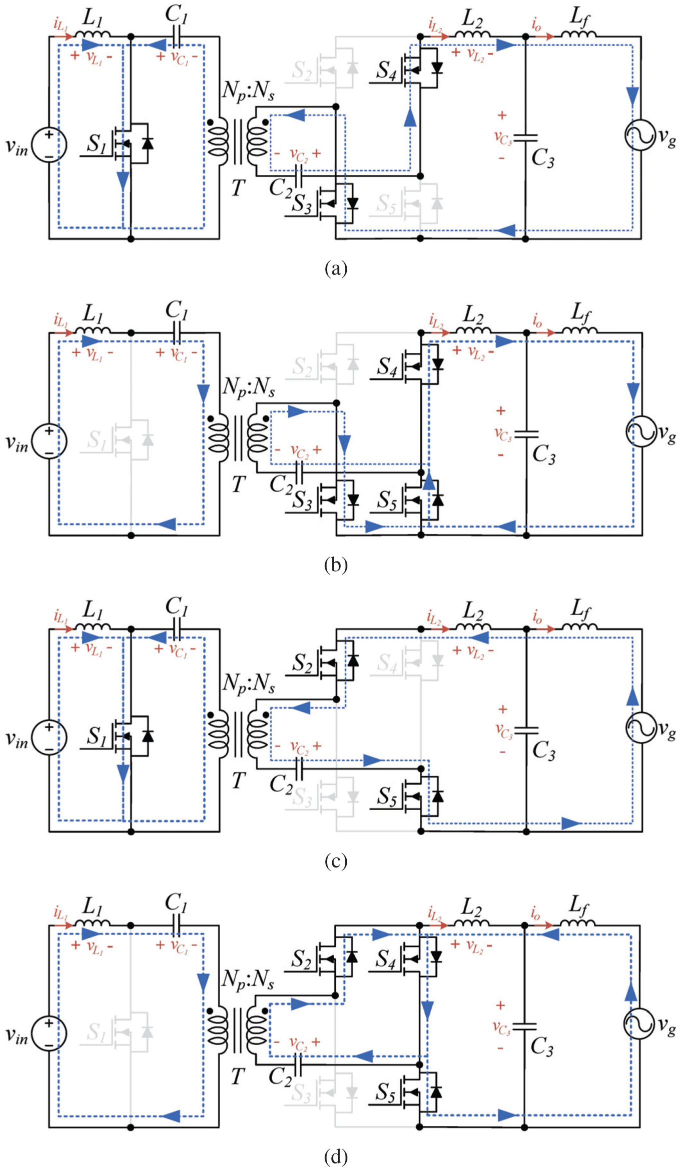

(a)
(b)
(c)
(d)

Fig. 3. Operating phases of the bridgeless Cuk-derived inverter. (a) Phase 1 in Sector I. (b) Phase 2 in Sector I. (c) Phase 1 in Sector IV. (d) Phase 2 in Sector IV.

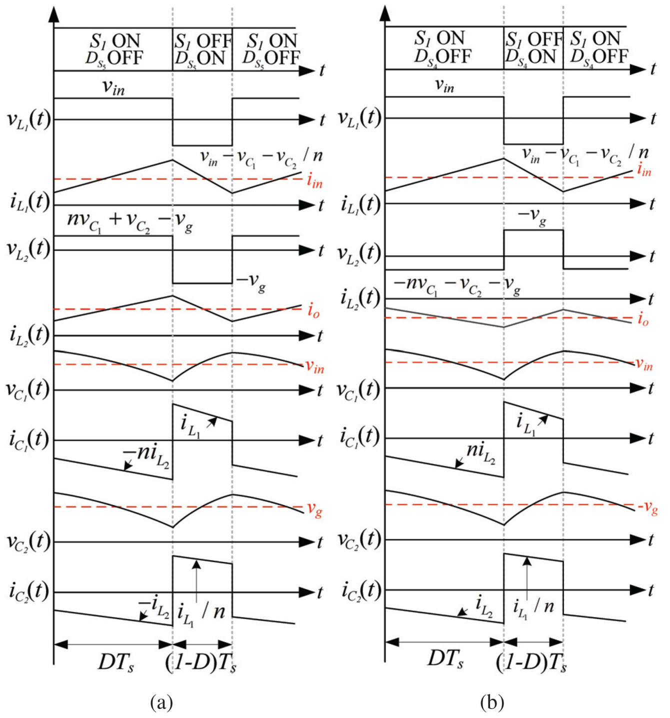

(a) (b)

Fig. 4. Theoretical waveforms of voltages and currents of inductors L_1 and L_2 and capacitors C_1 and C_2. (a) In Sector I. (b) In Sector IV.

direction as the grid voltage and is synchronized with it. The primary switch S_1 operates at high frequency with control duty-ratio d_c. In Sector I, switches S_3 and S_4 conduct during the switching period; the body diode of S_5 conducts in a complementary way to S_1. In Sector IV, switches S_2 and S_5 conduct during the switching period; the body diode of S_4 conducts in a complementary way to S_1.

In Sector I, the circuit experiences two phases per switching period: 1) S_1 turned ON; S_5 turned OFF [see Fig. 3(a)]; and 2) S_1 turned OFF; D_{S_5} turned ON [see Fig. 3(b)]. During the entire switching period, S_3 and S_4 are turned ON and S_2 is turned OFF. When S_1 is turned ON, the current flowing through L_1 increases and L_1 stores energy. C_1 discharges and its energy is transferred to the secondary side of the circuit through T. The transferred energy from C_1 and the energy in C_2 are moved to the output stage through L_2. When S_1 is turned OFF, the current flowing through L_1 decreases and its energy is transferred to C_1 and C_2. The energy in L_2 is transferred to the output grid while the current flows through L_2 and D_{S_5}. In Sector I, the theoretical waveforms of the proposed inverter in a switching cycle are shown in Fig. 4(a).

During Sector IV, the circuit also experiences two phases per switching period: 1) S_1 turned ON; S_4 turned OFF [see Fig. 3(c)]; and 2) S_1 turned OFF; D_{S_4} turned ON [see Fig. 3(d)]. During the entire switching period, S_2 and S_5 are turned ON and S_3 is turned OFF. Except for the states of switches S_2–S_5, the inverter in Sector IV operates in the same way as in Sector I. In Sector IV, the theoretical waveforms of the proposed inverter in a switching cycle are shown in Fig. 4(b).

The direction of the inductor current flow depends upon the average voltage across the inductor per switching cycle. During the ON-state and the OFF-state of S_1 in forward power flow, the inductor voltages v_{L_1}, v_{L_2} are given as

$$v_{L_1} = \begin{cases} v_{\text{in}} & \text{during the ON-state of } S_1 \\ v_{\text{in}} - v_{C_1} - v_{C_2}/n & \text{during the OFF-state of } S_1 \end{cases} \tag{1}$$

$$v_{L_2} = \begin{cases} nv_{C_1} + v_{C_2} - v_g & \begin{array}{c}\text{during the ON-state of } S_1 \\ \text{and } v_g > 0\end{array} \\ -nv_{C_1} - v_{C_2} - v_g & \begin{array}{c}\text{during the ON-state of } S_1 \\ \text{and } v_g < 0\end{array} \\ -v_g & \text{during the OFF-state of } S_1. \end{cases} \tag{2}$$

These voltages across L_1 and L_2 force the inductor currents i_{L_1} and i_{L_2} to yield forward power flow. Here, D is defined as

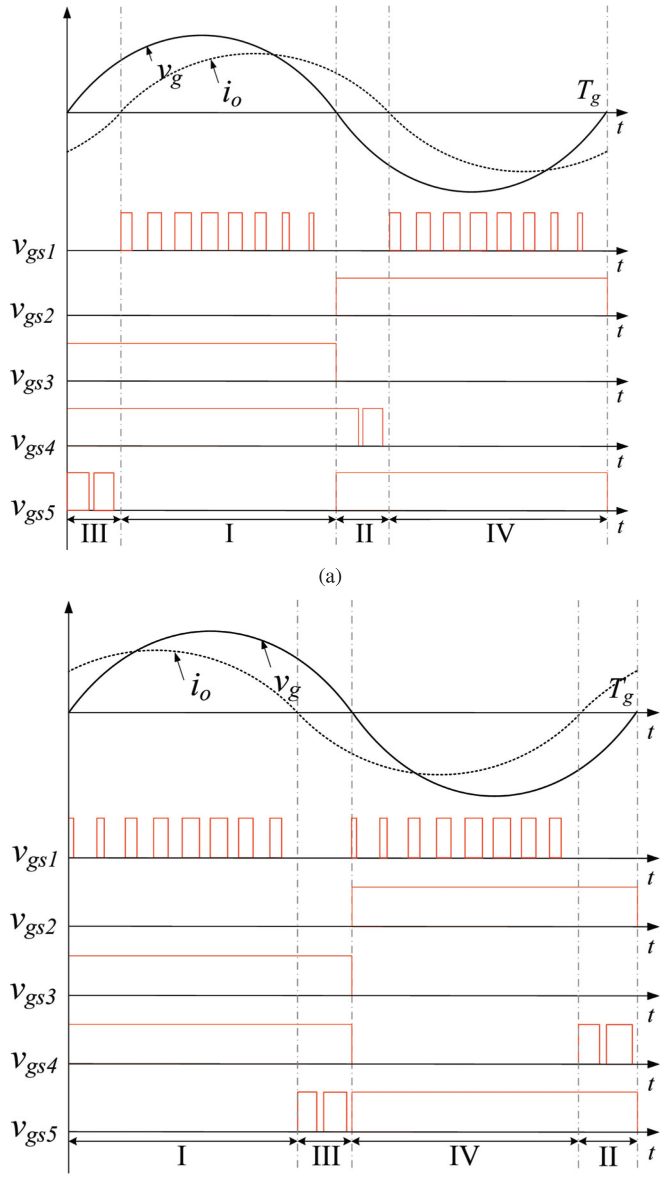

Fig. 5. Waveforms of gate drive signals for nonunity power factor operation. (a) Lagging power factor. (b) Leading power factor.

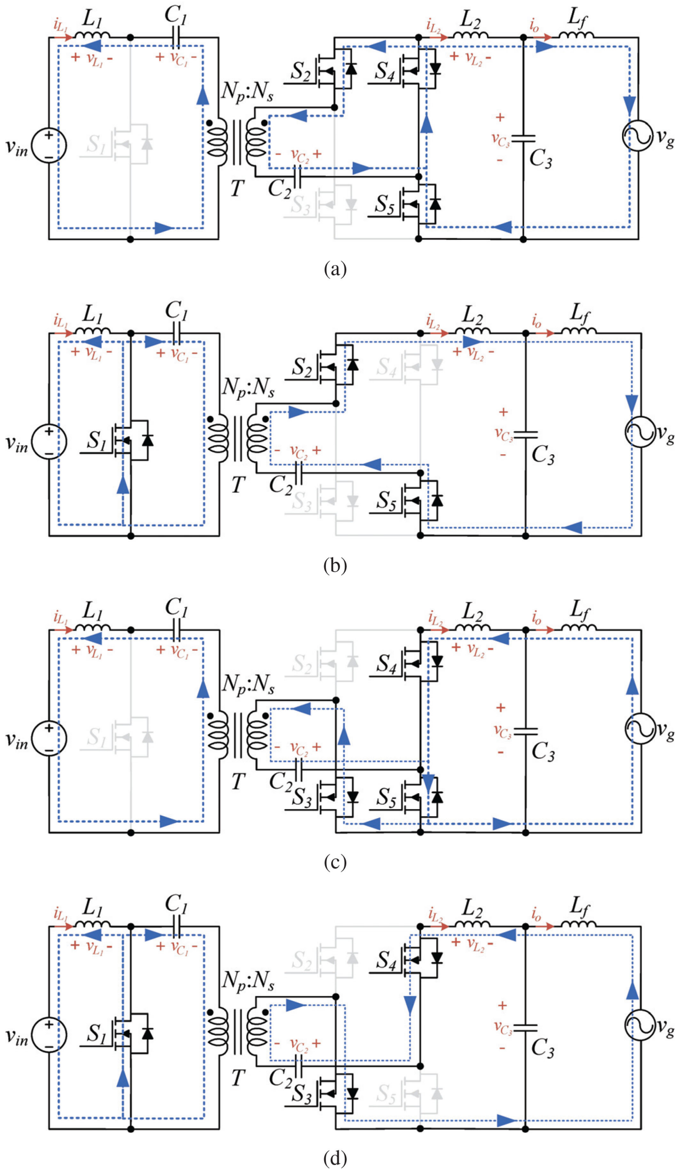

Fig. 6. Operating phases of the bridgeless Cuk-derived inverter. (a) Phase 1 in Sector II. (b) Phase 2 in Sector II. (c) Phase 1 in Sector III. (d) Phase 2 in Sector III.

the duty-ratio of S_1 in the steady state. The steady-state voltages v_{C_1} and v_{C_2} are computed as v_{in} and $|v_g|$ by using the inductor volt-second balance law [21]. Then, the voltage conversion ratio in forward power flow can be computed as

$$Dv_{\text{in}} - (1-D) \cdot (v_{\text{in}} - v_{C_1} - v_{C_2}/n) = 0 \tag{3}$$

$$D(nv_{C_1} + v_{C_2} - |v_g|) - (1-D)|v_g| = 0 \tag{4}$$

$$\frac{|v_g|}{v_{\text{in}}} = \frac{nD}{1-D} \left(= \frac{i_{L_1}}{|i_o|} \right). \tag{5}$$

2) Nonunity Power Factor: During the operation under nonunity power factor (see Fig. 5), the grid current is phase-leaded or phase-lagged to the grid voltage. When outputting lagging power factor, the inverter has four operating sequences during the grid period: III → I → II → IV; when outputting leading power factor, it has four operating sequences during the grid period: II → I → III → IV (see Fig. 5). In Sectors I and IV, the operating principles of the operation under nonunity power factor are the same as those under unity power factor. The following is about the detailed switching operation in Sectors II and III. Switch S_4 operates at high frequency with control duty-ratio $1 - d_c$, and switches S_2 and S_5 conduct during the switching period in Sector II; switch S_5 operates at high frequency with control duty-ratio $1 - d_c$, and switches S_3 and S_4 conduct during the switching period in Sector III. The body diode of S_1 conducts in a complementary way to S_4 or S_5 switching at high frequency both in Sectors II and III.

In Sector II, the circuit experiences two phases per switching period: 1) S_4 turned ON; S_1 turned OFF [see Fig. 6(a)]; and 2)

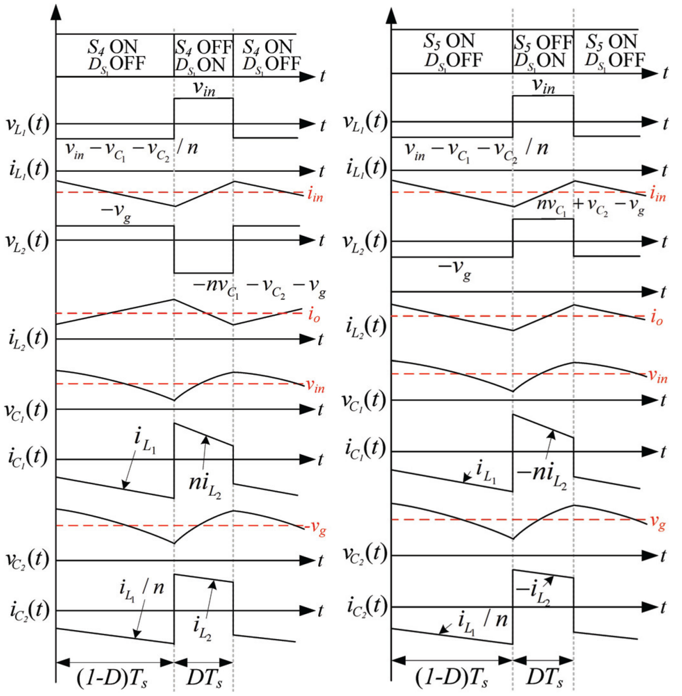

(a) (b)

Fig. 7. Theoretical waveforms of voltages and currents of inductors L_1 and L_2 and capacitors C_1 and C_2. (a) In Sector II. (b) In Sector III.

S_4 turned OFF; D_{S_1} turned ON [see Fig. 6(b)]. During the entire switching period, S_2 and S_5 are turned ON and S_3 is turned OFF. When S_4 is turned ON, the current flowing through L_2 increases and it stores energy. C_2 discharges and its energy is transferred to the primary side of the circuit through T. The transferred energy from C_2 and the energy in C_1 are moved to the input stage through L_1. When S_4 is turned OFF, the current flowing through L_2 decreases and its energy is transferred to C_1 and C_2. The energy in L_1 is transferred to the input, while the current flows through L_2 and D_{S_1}. In Sector II, the theoretical waveforms of the proposed inverter in a switching cycle are shown in Fig. 7(a).

In Sector III [see Fig. 7(b)], the circuit also goes through two phases per switching period: 1) S_5 turned ON; S_1 turned OFF [see Fig. 6(c)]; and 2) S_5 turned OFF; D_{S_1} turned ON [see Fig. 6(d)]. During the entire switching period, S_3 and S_4 are turned ON and S_2 is turned OFF. Except for the states of switches S_2–S_5, the inverter in Sector III operates in the same way as in Sector II. In Sector III, the theoretical waveforms of the proposed inverter in a switching cycle are shown in Fig. 7(b).

During the ON-state and the OFF-state of S_4 or S_5 in reverse power flow, the inductor voltages v_{L_1}, v_{L_2} are

$$v_{L_1} = \begin{cases} v_{\text{in}} - v_{C_1} - v_{C_2}/n & \text{during the ON-state of } S_4 \\ & (v_g < 0) \text{ or } S_5\ (v_g > 0) \\ v_{\text{in}} & \text{during the OFF-state of } S_4 \\ & (v_g < 0) \text{ or } S_5\ (v_g > 0) \end{cases} \tag{6}$$

$$v_{L_2} = \begin{cases} -v_g & \text{during the ON-state of } S_4 \\ & (v_g < 0) \text{ or } S_5\ (v_g > 0) \\ -nv_{C_1} - v_{C_2} - v_g & \text{during the OFF-state of } S_4 \\ & (v_g < 0) \\ nv_{C_1} + v_{C_2} - v_g & \text{during the OFF-state of } S_5 \\ & (v_g > 0). \end{cases} \tag{7}$$

The above voltages across L_1 and L_2 force inductor currents i_{L_1} and i_{L_2} to yield reverse power flow. The steady-state duty-ratio of the secondary-side switches S_4 (in Sector II) or S_5 (in Sector III) is $1 - D$. Accordingly, the voltage conversion ratio is the same as that in the forward power flow.

III. CONTROL DESIGN

The goal of the control system (see Fig. 8) of the grid-connected bridgeless Cuk-derived inverter is to make its output current track the reference current as closely as possible. The Cuk-derived topology has two right-half-plane (RHP) zeros in its transfer function [21]. The topology also suffers from time-varying grid-voltage disturbance when connected to the grid. To obtain precise output current tracking, an RC coupled with a linear feedback controller plus feed-forward controller is used. The reference output current and the output current are also redefined for the control purpose; these changes simplify the duty-cycle modulation block design that is followed by the dynamic control block. Moreover, the physical implementation of the modulation scheme is represented for active-/reactive-power transfer in accordance with the operating sector in Fig. 8. Also, to reduce the conduction loss due to the use of body diode, the use of SR technique is discussed at the end of this section.

First, it is assumed that the grid voltage $v_g = V_m \sin(\omega_g k T_s)$ and the reference output current $i_{\text{o\_ref}} = I_m \sin(\omega_g k T_s + \phi)$, where V_m is the peak value of the grid voltage, I_m the peak value of the reference output current, k the discrete time index, T_s the switching period, ω_g the grid angular frequency, and ϕ the phase difference between v_g and $i_{\text{o\_ref}}$. The proposed modulation technique makes the circuit have equivalent operation in positive and negative half-cycles of the grid, while maintaining the power-flow direction. In turn, the reference output current should be in reverse during the negative half cycle of the grid. The resulting output current i_o and its reference $i_{\text{o\_ref}}$ can be represented as

$$i_o^* \text{ (or } i_{\text{o\_ref}}^*) = \begin{cases} |i_o| \text{ (or } |i_{\text{o\_ref}}|) & \text{in Sector I} \\ & \text{or Sector IV} \\ -|i_o| \text{ (or } -|i_{\text{o\_ref}}|) & \text{in Sector II} \\ & \text{or Sector III.} \end{cases} \tag{8}$$

The modified currents are used to generate an error signal of the dynamic control block in the bridgeless Cuk-derived inverter.

Neglecting the effect of the output filter, the output current i_o can be considered as the inductor current i_{L_2}. The equation of the averaged voltage across L_2 over a switching period T_s can

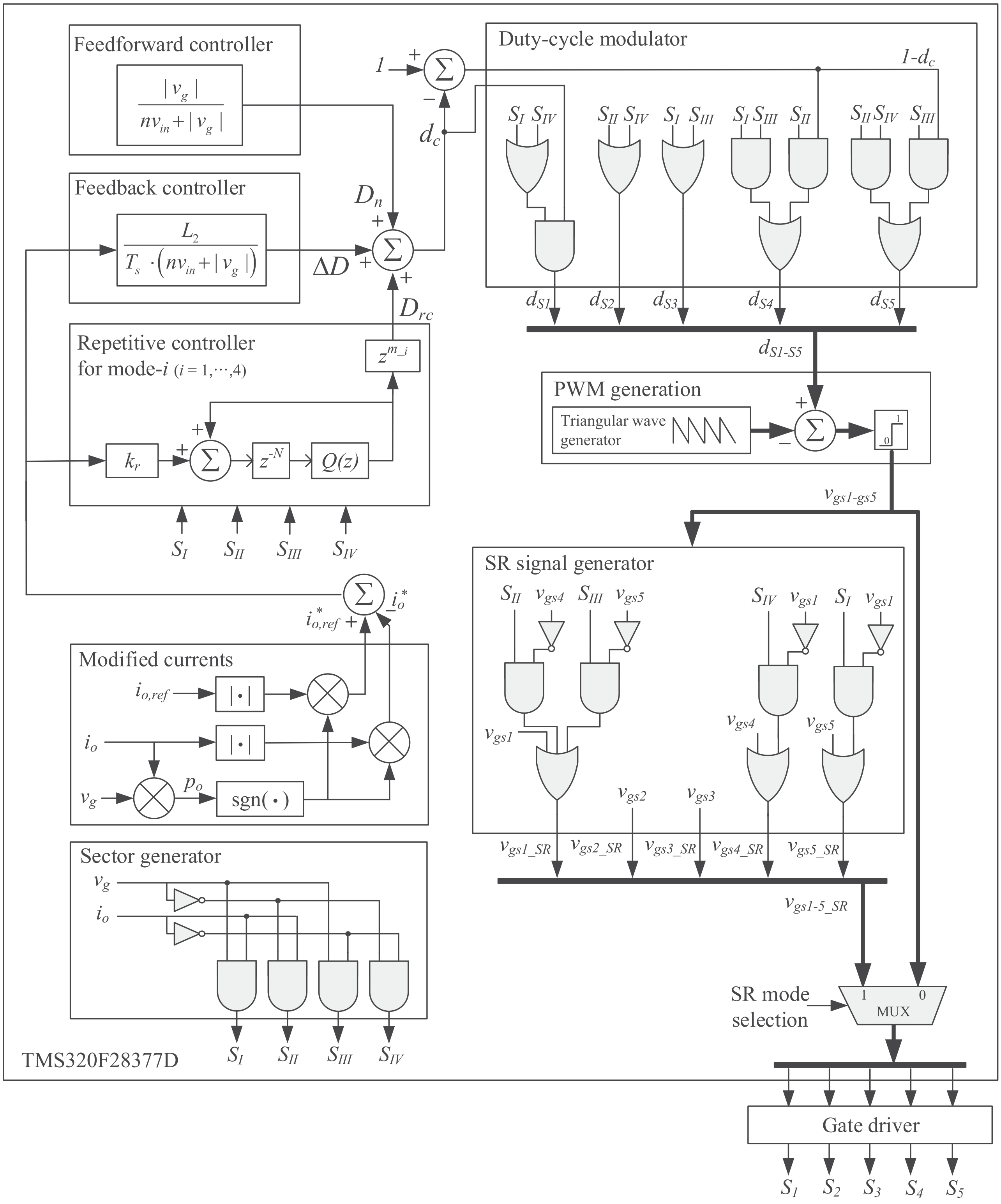

Fig. 8. Schematic of the overall control system for the bridgeless Cuk-derived single power conversion inverter.

be derived as

$$DT_s \cdot (nv_{C_1} + v_{C_2} - |v_g|) - (1 - D)T_s \cdot |v_g| = L_2 \Delta i_o^* \quad (9)$$

where Δi_o^* is the current variation of i_o^*. The steady-state v_{C_1} and v_{C_2} are v_{in} and $|v_g|$, respectively, by the principle of inductor volt-second balance [21] and rearranging yields

$$D = \frac{|v_g|}{nv_{\text{in}} + |v_g|} + \frac{L_2}{nv_{\text{in}} + |v_g|} \cdot \frac{\Delta i_o^*}{T_s}. \quad (10)$$

Substituting $v_g = V_m \sin(\omega_g kT_s)$ with the grid angular frequency ω_g into (10) yields

$$D = \frac{|V_m \sin(\omega_g kT_s)|}{nv_{\text{in}} + |V_m \sin(\omega_g kT_s)|} + \frac{L_2}{nv_{\text{in}} + |V_m \sin(\omega_g kT_s)|} \cdot \frac{\Delta i_o^*(kT_s)}{T_s} = D_n(kT_s) + \Delta D(kT_s). \tag{11}$$

To make the output current track the reference output current, the current variation can be set as $\Delta i_o^* = i_{\text{o\_ref}}^* - i_o^*$. Then, the nominal duty-ratio D_n is

$$D_n((k+1)T_s) = \frac{|V_m \sin(\omega_g kT_s)|}{nv_{\text{in}} + |V_m \sin(\omega_g kT_s)|} \tag{12}$$

and the duty-ratio variation ΔD is

$$\Delta D((k+1)T_s) = \frac{L_2}{nv_{\text{in}} + |V_m \sin(\omega_g kT_s)|} \cdot \frac{i_{\text{o\_ref}}^*(kT_s) - i_o^*(kT_s)}{T_s}. \tag{13}$$

To reduce the burden from the feedback controller, D_n is used as a feedforward control input. Then, ΔD directly contributes to the output feedback current control.

However, the feedforward controller and the linear feedback controller $D_n + \Delta D$ cannot accurately control the bridgeless Cuk-derived inverter because of the RHP zeros in the Cuk-derived topology. Also, it suffers from time-varying grid voltage disturbance. To obtain precise tracking of the output current, an RC with phase-lead compensator [21], [22] is adopted. Here, the dynamics of the bridgeless Cuk-derived inverter differs depending on the operating sectors classified according to the polarities of v_g and i_o (see Table II). Thus, an RC with phase-lead compensator should be designed appropriately for each sector. The repetitive control input for Sector-ρ ($\in \{1, 2, 3, 4\}$) is described as

$$D_{\text{rc}} = \left(k_{r\_\rho} \cdot z^{m\_\rho} \frac{z^{-N}Q(z)}{1 - z^{-N}Q(z)}\right) \cdot \left(i_{\text{o\_ref}}^*(z) - i_o^*(z)\right) \quad \text{for } \rho = 1, \ldots 4 \tag{14}$$

where k_{r_ρ} is the RC gain for ρ; $N = f_s/f_g$ where $f_s = 1/T_s$ is the switching frequency and f_g the reference frequency; z^{m_ρ} is the phase-lead compensation term to compensate for the phase lag caused by the RHP zeros for ρ; $Q(z)$ is the low-pass filter to ensure the system's robustness, and it is designed as a p-order finite impulse response filter with zero phase shift. One has the following:

$$Q(z) = \Sigma_{i=0}^{p} \alpha_i z^i + \Sigma_{i=1}^{p} \alpha_i z^{-i} \tag{15}$$

where $\alpha_0 + 2\Sigma_{i=1}^{p} \alpha_i = 1$ with $\alpha_i > 0$ and p the number of samples used for filtering. Then, the repetitive control input D_{rc} combines with $D_n + \Delta D$ to form the control duty-cycle d_c.

To control five switches S_{1-5} with only one d_c, the duty-cycle required for each switch should be changed according to the gate driving rules as in Section II. To generate different duty-cycles for S_{1-5}, the control input duty-ratio d_c is injected into the duty-ratio generation module (see Fig. 8). Then, the resultant signals are compared with a triangular carrier wave, and the compared signal is used to generate the gate signals of S_1, S_2, S_3, S_4, and S_5. Finally, d_c is used as the duty-ratio of S_1 in forward power flow, and $1 - d_c$ is used as the duty-ratio of S_4 or S_5 in reverse power flow.

The conduction loss can be further reduced by using SR technique instead of using the body diode itself. When the proposed inverter operates in CCM, SR technique can be applied to S_1, S_4, or S_5 for each sector; S_1 operates in a complementary way to S_4 in Sector II, and to S_5 in Sector III. S_4 operates in a complementary way to S_1 in Sector IV, and S_5 operates in a complementary way to S_1 in Sector I (see Fig. 8). Then, the gate signal for each of switches S_{1-5} is determined according to the selection of an SR operation mode ("ON" or "OFF").

For practical SR implementation, the dead time of SR switch should be set appropriately. Long dead time would result in additional losses due to the conduction and reverse recovery of the body diode. On the other hand, short dead time would lead to undesired simultaneous conduction of the switches and a consequent loss. An ideal SR turn-ON dead time is the time taken by the voltage across the SR to reach zero; an ideal SR turn-OFF dead time is the time taken by the current through the SR to drop to zero [30]. By measuring the voltage and current of the SR switch, an ideal SR dead time can be obtained, but it requires additional sensors. To calculate the optimal dead time for the SR switch without using the sensors, the duty-ratio minimization algorithm [31], the input minimization algorithm [32], and the perturbation-based extremum seeking algorithm [33] have been introduced to obtain the optimal dead time for the SR switch. However, it would increase the complexity of the overall control system. Here, the dead time is relatively short as compared to the commutation time of the SR, given that the switching frequency is 40 kHz. Therefore, in this paper, the fixed dead time driving strategy is adopted as that in [34]. For instance, in Sector I, the dead time $t_{\text{d\_SR\_off}}$ during turn-OFF can be simply described as the summation of the time to discharge the parasitic switch node capacitance C_{S_5} of S_5 and the intrinsic turn-OFF delay $t_{\text{off\_d}}$ of S_1 [34] as

$$t_{\text{d\_SR\_off}} = \frac{nv_{C_1} + v_{C_2}}{i_{L_2}} \cdot C_{S_5} + t_{\text{off\_d}}. \tag{16}$$

The dead time $t_{\text{d\_SR\_off}}$ is set to satisfy the worst-case condition, in which the inverter operates at the instantaneous peak point. On the other hand, the dead time $t_{\text{d\_SR\_on}}$ during turn-ON is set to be small enough to prevent the conduction overlap of S_1 and S_5 during the CCM operation [33].

Remark 1: Let us define V_{dc} as the input voltage of an H-bridge inverter. In a conventional H-bridge inverter with bipolar modulation method, the output voltage of the inverter switches between V_{dc} and $-V_{\text{dc}}$ when $v_g > 0$, and between $-V_{\text{dc}}$ and V_{dc} when $v_g < 0$ during the switching period. The voltage difference is high enough to generate the reactive current with any desired power factor and supply it to the grid. On the other hand, in a conventional H-bridge inverter with unipolar modulation method, the output voltage of the inverter switches between V_{dc} and 0 when $v_g > 0$, and between $-V_{dc}$ and 0 when $v_g < 0$ during the switching period. The voltage difference is not high enough to generate the reactive current near the zero grid voltage [10], [11].

TABLE III
PEAK CURRENT, PEAK VOLTAGE, AND AVERAGE CURRENT OF THE SWITCHES

Sector I	Sector IV	Voltage/Current	Values
S_1		On-state minimum current	$\frac{\lvert i_o\rvert}{v_{in}}\left(\lvert v_g\rvert+nv_{in}\right)-\frac{v_{in}T_s}{2}\frac{\lvert v_g\rvert}{nv_{in}+\lvert v_g\rvert}\left(\frac{1}{L_1}+\frac{n^2}{L_2}\right)$
		On-state maximum current	$\frac{\lvert i_o\rvert}{v_{in}}\left(\lvert v_g\rvert+nv_{in}\right)+\frac{v_{in}T_s}{2}\frac{\lvert v_g\rvert}{nv_{in}+\lvert v_g\rvert}\left(\frac{1}{L_1}+\frac{n^2}{L_2}\right)$
		Off-state voltage	$v_{in}+\frac{\lvert v_g\rvert}{n}$
S_3	S_2	On-state current	$\lvert i_o\rvert$ during S_1 on-state, $\frac{\lvert i_o\rvert\cdot\lvert v_g\rvert}{nv_{in}}$ during S_1 off-state,
S_4	S_5	On-state current	$\lvert i_o\rvert$
S_5	S_4	On-state minimum current	$\frac{\lvert i_o\rvert}{nv_{in}}\left(\lvert v_g\rvert+nv_{in}\right)-\frac{v_{in}T_s}{2}\frac{\lvert v_g\rvert}{nv_{in}+\lvert v_g\rvert}\left(\frac{1}{nL_1}+\frac{n}{L_2}\right)$
		On-state maximum current	$\frac{\lvert i_o\rvert}{nv_{in}}\left(\lvert v_g\rvert+nv_{in}\right)+\frac{v_{in}T_s}{2}\frac{\lvert v_g\rvert}{nv_{in}+\lvert v_g\rvert}\left(\frac{1}{nL_1}+\frac{n}{L_2}\right)$
		Off-state voltage	$nv_{in}+\lvert v_g\rvert$

A conventional H-bridge inverter with unipolar modulation can generate the required reactive current when the desired power factor is high; this inverter would generate highly distorted reactive current when the desired power factor is low.

Similar to a conventional H-bridge inverter with unipolar modulation method, an H-bridge that consists of S_2–S_5 in the proposed inverter outputs $nv_{C_1}+v_{C_2}$ and 0 when $v_g>0$, and outputs $-nv_{C_1}-v_{C_2}$ and 0 when $v_g<0$. A similar tendency can be observed in the proposed inverter. To analyze the reactive-power-transfer ability of the proposed inverter in detail, two cases are considered as follows: 1) when the desired power factor is leading; and 2) when the desired power factor is lagging. When the desired power factor is leading, S_1 mainly operates in forward power flow, and S_4 or S_5 mainly operates in reverse power flow. Here, D is defined as the duty-ratio of S_1 and $\bar{D}(=1-D)$ as the duty-ratio of S_4 or S_5 in the steady state. In reverse power flow, $\bar{D}$ can be described as

$$\bar{D}=1-D=\frac{nv_{\text{in}}}{nv_{\text{in}}+|v_g|}-\frac{L_2}{nv_{\text{in}}+|v_g|}\cdot\frac{\Delta i_o^*}{T_s} \tag{17}$$

where Δi_o^* is the required current variation of i_o^* to track the modified reference output current $i_{\text{o\_ref}}^*$ in (8). When the desired power factor is leading, the output Δi_o^* in reverse power flow is negative. When the grid voltage is close to zero, the required duty-ratio $\bar{D}$ of S_4 or S_5 becomes larger than one if

$$|v_g|<-L_2\cdot\frac{\Delta i_o^*}{T_s}. \tag{18}$$

Since the duty-ratio $\bar{D}$ is limited to one, the grid voltage is not enough to magnetize the output inductor, which leads to the distorted output current around the zero grid-voltage. When the desired power factor was not low, time interval with $\bar{D}=1$ was short, and the current distortion was not significant. However, as the power factor gets lower, the time interval with $\bar{D}=1$ gets longer, and the current distortion becomes more significant. Thus, the capability for the reactive-power injection in the proposed inverter is limited. When the desired power factor is lagging, Δi_o^* in reverse power flow is positive. Then, the required duty ratio $\bar{D}$ is lower than one. Therefore, the output current distortion is relatively insignificant around zero grid voltage [10].

IV. DESIGN CONSIDERATION

A. Transformer

The loss caused by the switches can be obtained from ON-state currents and OFF-state voltage (see Table III). The transformer's turns-ratio n mainly affects the switching loss and the conduction loss of the switches in the bridgeless Cuk-derived inverter. The loss caused by the switches comprises most of the overall power conversion losses (see Fig. 22), so the transformer's turns-ratio n should be designed to minimize the loss in switches while maintaining the voltage conversion ratios (5) during a grid period. For a simple analysis, it is assumed that the inverter operates under SR mode, and the conduction and switching losses are considered in the loss caused by the switches. Then, the averaged loss caused by the switches during a grid period can be derived as

$$P_{\text{s\_av}}(n,L_{\text{eq}})=\frac{1}{T_s}\int_0^{T_s}P_s(i_o(t),v_g(t),n,L_{\text{eq}})dt \tag{19}$$

where $L_{\text{eq}}=L_1L_2/(n^2L_1+L_2)$ is the equivalent inductance, and the loss caused by the switches is $P_s=\sum_{i=1}^{5}(P_{\text{s\_cond}}^{(i)}+P_{\text{s\_sw}}^{(i)})$; $P_{\text{s\_cond}}^{(i)}$ and $P_{\text{s\_sw}}^{(i)}$ are, respectively, the conduction and switching losses of S_i for $i=1,\ldots,5$.

From (19), the averaged loss can be obtained using the current and voltage of switches (see Table III), and the resulting averaged loss depends upon turns ratio n and equivalent inductance L_{eq} (see Fig. 9). The loss in the switches increases if $n>3.3$ or $n<3$. As the inductance increases, the loss in the switches decreases, but this change results in increasing the size of inductors, but with inductance >70 μH, the equivalent inductance does not greatly affect the loss in the switches. Thus, it is regarded that the appropriate n is $n=3.1$ and that the minimum equivalent inductance $L_{\text{eq,min}}$ is 70 μH in the prototype implementation.

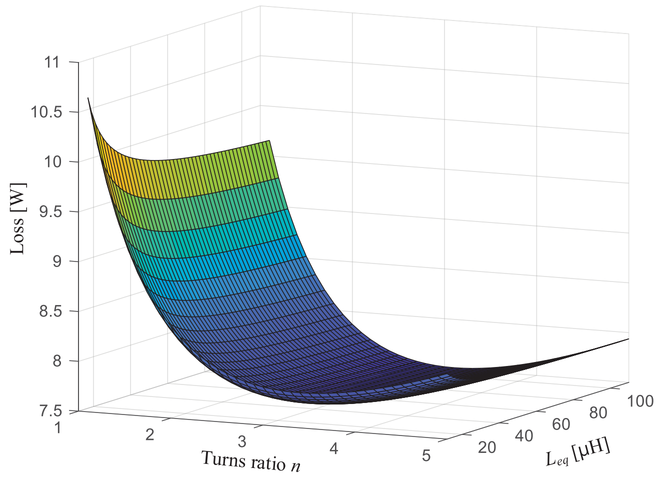

Fig. 9. Overall loss on switches in a grid period depending on the turns ratio n and the equivalent inductance L_{eq}.

TABLE IV
PARAMETERS AND COMPONENTS OF THE PROTOTYPE BRIDGELESS CUK-DERIVED INVERTER

Parameters	Symbols	Values
Input voltage	V_i	60 Vdc
Grid voltage	v_g	220 V_{rms}
Grid frequency	f_g	60 Hz
Switching frequency	f_s	40 kHz
First capacitance	C_1	8.8 μF
Second capacitance	C_2	200 nF
Third capacitance	C_3	470 nF
First inductance	L_1	360 μH
Second inductance	L_2	1.1 mH
Filter inductance	L_f	170 μH
Turns ratio of T	$N_p : N_s$	10:31
Magnetic inductance of T	L_m	65 μH
Leakage inductance of T	L_{lk}	0.25 μH
Components	**Symbols**	**Part numbers**
Primary-side switch	S_1	IPP200N25N3G
Secondary-side switches	$S_2 - S_5$	IPW60R070F7
Transformer core	T	PQ3535 (Ferrite R)

Considering the resulting transformer's turns-ratio $n = 3.1$ and the characteristic of the transformer core provided in Table IV, the appropriate number of the primary turns and secondary turns of the transformer are selected as $n_p = 10$ and $n_s = 31$. Also, the energy stored in the leakage inductance of the transformer can generate the voltage spike at the main switch. To minimize the leakage inductance of the transformer, a sandwich winding technique [35] is adopted in the transformer.

B. Inductors L_1 and L_2

An allowable maximum ripple current $\Delta i_{L_2,\max}$ at the instantaneous maximum power can determine the inductance L_2 as [37] follows:

$$L_2 = \frac{T_s v_{L_2} D}{\Delta i_{L_2}} = \frac{T_s\left(n v_{C_1} + v_{C_2} - |v_g|\right)}{\Delta i_{L_2}} \cdot \left(\frac{|v_g|}{n v_{\text{in}} + |v_g|}\right)$$
$$\geq L_{2,\min} = \frac{T_s v_{L_2} D_{\max}}{\Delta i_{L_2,\max}} = \frac{T_s n v_{\text{in}} V_m}{\Delta i_{L_2,\max}\left(n v_{\text{in}} + V_m\right)}. \quad (20)$$

where $D_{\max}$ is the nominal duty-ratio at the instantaneous maximum power.

Setting the maximum ripple current as 80% of the maximum value of i_{L_2}, $L_{2,\min}$ is calculated as

$$L_{2,\min} = \frac{2.5 \times 10^{-5} \times 3.1 \times 60 \times 311}{0.8 \times 3.23 \times (3.1 \times 60 + 311)} = 1.1\,\text{mH}. \quad (21)$$

Likewise, an allowable maximum ripple current $\Delta i_{L_1,\max}$ at the instantaneous maximum power can determine the inductance L_1 as

$$L_1 \geq L_{1,\min} = \frac{T_s v_{L_1} D_{\max}}{\Delta i_{L_1,\max}} = \frac{T_s v_{\text{in}} V_m}{\Delta i_{L_1,\max}\left(n v_{\text{in}} + V_m\right)}. \quad (22)$$

Setting the maximum ripple current as 20% of the maximum value of i_{L_1}, $L_{1,\min}$ is calculated as

$$L_{1,\min} = \frac{2.5 \times 10^{-5} \times 60 \times 311}{0.2 \times 16.67 \times (3.1 \times 60 + 311)} = 281\,\mu\text{H}. \quad (23)$$

Hence, the appropriate inductances L_1 and L_2 are selected as $L_1 = 360\ \mu$H and $L_2 = 1.1$ mH such that $L_{\text{eq}} = 86.85\ \mu$H is more than the minimum equivalent inductance $L_{\text{eq,min}} = 70\ \mu$H.

C. Intermediate Capacitors C_1 and C_2

An allowable maximum ripple voltage $\Delta v_{C_1,\max}$ at the instantaneous maximum power can determine the capacitance C_1 as [37] follows:

$$C_1 \geq C_{1,\min} = \frac{T_s i_{C_1} D_{\max}}{\Delta v_{C_1,\max}} = \frac{T_s n I_m}{\Delta v_{C_1,\max}} \cdot \left(\frac{V_m}{V_m + n v_{\text{in}}}\right). \quad (24)$$

In order to make the voltage across C_1 become almost constant within a switching period and its voltage ripple become less than 30% of the input voltage, $C_{1,\min}$ is calculated as

$$C_{1,\min} = \frac{2.5 \times 10^{-5} \times 3.1 \times 3.23}{0.3 \times 60} \cdot \left(\frac{311}{311 + 3.1 \times 60}\right)$$
$$= 8.7\,\mu\text{F}. \quad (25)$$

Likewise, an allowable maximum ripple voltage $\Delta v_{C_2,\max}$ at the instantaneous maximum power can determine the capacitance C_2 as

$$C_2 \geq C_{2,\min} = \frac{T_s i_{C_2} D_{\max}}{\Delta v_{C_2,\max}} = \frac{T_s I_m}{\Delta v_{C_2,\max}} \cdot \left(\frac{V_m}{V_m + n v_{\text{in}}}\right). \quad (26)$$

In order to make the maximum ripple voltage become less than 85% of the maximum voltage of v_{C_2}, $C_{2,\min}$ is calculated as

$$C_{2,\min} = \frac{2.5 \times 10^{-5} \times 3.23}{0.85 \times 311} \cdot \left(\frac{311}{311 + 3.1 \times 60}\right) = 191\,\text{nF}. \quad (27)$$

Hence, the appropriate capacitances C_1 and C_2 are selected as $C_1 = 8.8\,\mu$F and $C_2 = 200$ nF, which are more than the minimum capacitances $C_{1,\min}$ and $C_{2,\min}$.

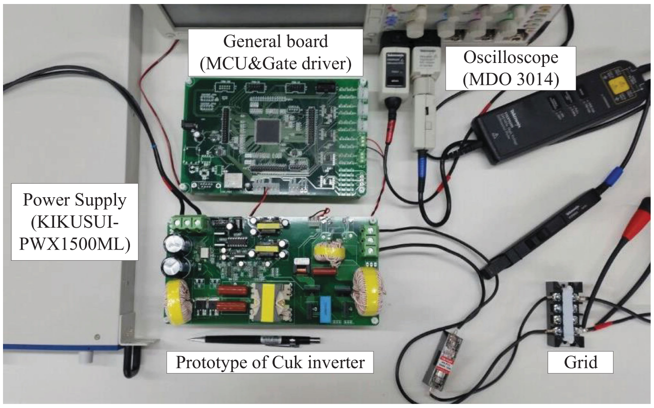

Fig. 10. Experimental setup of the bridgeless Cuk-derived inverter system.

D. Capacitor C_3 and Filter Inductor L_f

As the *LCL* filter features good decoupling from the grid impedance, and good current ripple attenuation even with the small inductance value, this filter is suited for the grid-connected inverter. Its design procedure is introduced in [38]. To attain sufficient switching ripple attenuation, the cut-off frequency should be lower than half of the switching frequency. The cut-off frequency can be calculated as

$$f_{LC,\text{cut}} = \frac{1}{2\pi}\sqrt{\frac{L_2+L_f}{L_2L_fC_3}} \le \frac{f_s}{2}. \tag{28}$$

The maximum power-factor variation can determine capacitance C_3 as

$$C_3 \le C_{3,\max} = \frac{I_m}{2\pi f_g V_m}\tan\theta \tag{29}$$

where θ is the displacement angle between the grid voltage and the output current. Here, C_3 is designed such that the reactive power absorbed from C_3 becomes $\le 1\%$ of the rated power.

The corresponding value of L_f is

$$\begin{aligned} L_f \ge L_{f,\min} &= \frac{L_2}{f_s^2\pi^2L_2C_3 - 1} \\ &= \frac{1.1\times10^{-3}}{40\times10^3\times\pi^2\times1.1\times10^{-3}\times470\times10^{-9}-1} \\ &= 153.54\ \mu\text{H}. \end{aligned} \tag{30}$$

Hence, the appropriate inductance L_f is selected as $L_f = 170\ \mu$H, which are more than $L_{f,\min}$.

V. Experimental Results and Discussion

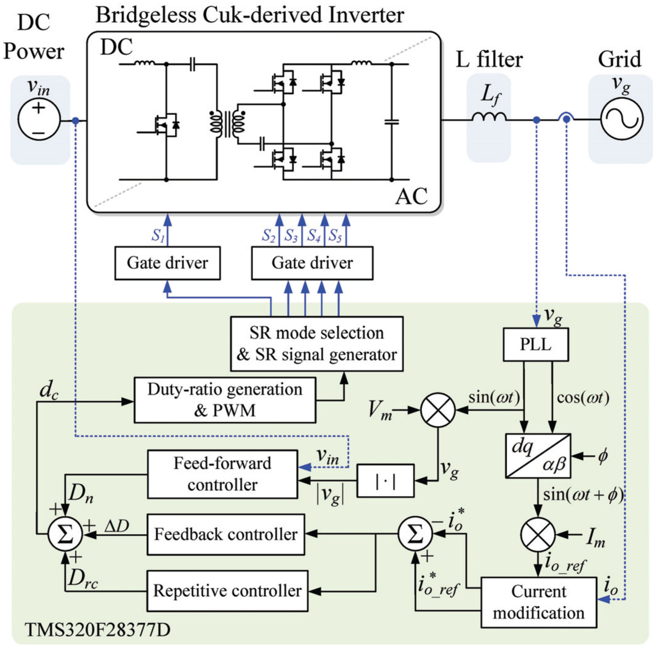

Fig. 11. Configuration of the proposed control system.

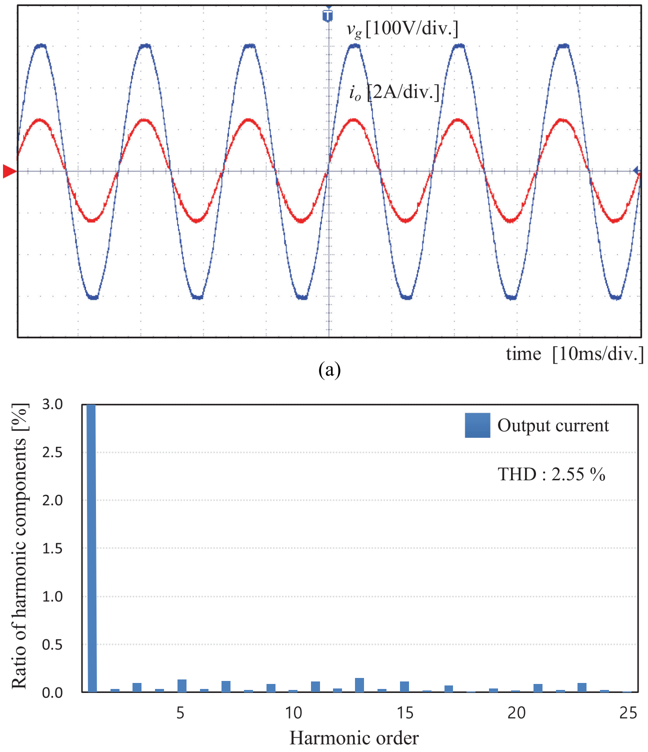

(a)

(b)

Fig. 12. Experimental results when the bridgeless Cuk-derived inverter operates at unity power factor. (a) Experimental waveforms of the grid voltage and the output current. (b) Frequency spectrum of the output current.

A prototype (see Table IV and Fig. 10) of the 500-VA experimental bridgeless Cuk-derived inverter was constructed for the experimental validation of the developed design rules. The control algorithms were implemented on a TMS320F28377D digital signal processor chip; a single-phase phase-locked loop with a notch filter [39] was used for grid voltage synchronization (see Fig. 11). In this experiment, the reference output current was obtained using the dq–$\alpha\beta$ transformation, and the modified currents i_o^* and $i^*_{o\_\text{ref}}$ were generated in accordance with rule (8). All the system parameters were designed according to the design guideline (see Section IV).

The combination of the feedback current controller plus the feedforward controller is not sufficient to track the output current

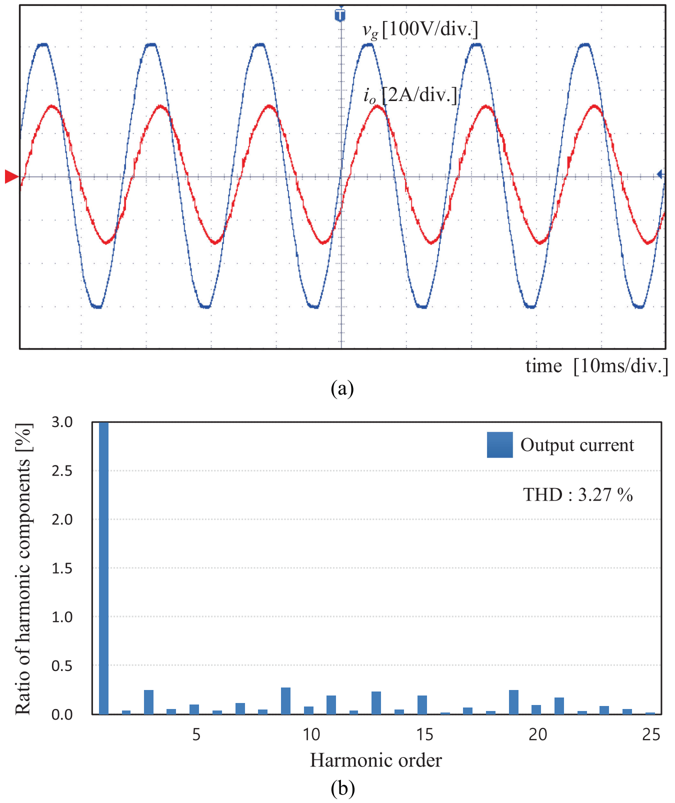

Fig. 13. Experimental results when the bridgeless Cuk-derived inverter operates at 0.85 lagging power factor. (a) Output waveforms of the grid voltage and output current. (b) Frequency spectrum of the output current.

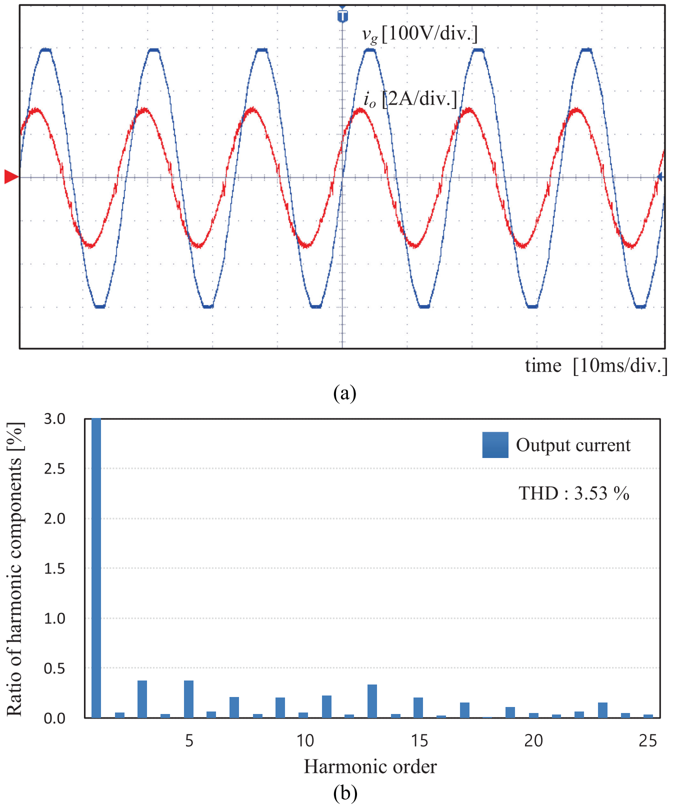

Fig. 14. Experimental results when the bridgeless Cuk-derived inverter operates at 0.85 leading power factor. (a) Output waveforms of the grid voltage and output current. (b) Frequency spectrum of the output current.

with sufficient precision. Thus, the RC is used and designed in accordance with the four sectors. In the RCs, the RC gain k_r was selected as $0 < k_r < 1$, and the cut-off frequency of the filter $Q(z)$ was set to 13.2 kHz to obtain tracking performance in a wide frequency band; $Q(z) = 0.1z + 0.8 + 0.1z^{-1}$. The RC gains and the phase-lead steps for each sector are given as $k_{r\_1-4} = 0.1$, $m_1 = m_4 = 4$, and $m_2 = m_3 = 2$.

When the bridgeless Cuk-derived inverter operated under unity power factor, the output current tracked the reference without any visible distortions and was in phase with the corresponding grid voltage [see Fig. 12(a)]. The frequency spectrum of the output current with unity power factor and its THD was 2.62%, which satisfies the IEEE-1547 requirements (THD $\leq$ 5%) [40].

When the bridgeless Cuk-derived inverter operated under nonunity power factor, the bridgeless Cuk-derived inverter accurately generated the phase-lagged/leaded output current [see Figs. 13(a) and 14(a)]; the corresponding phase angle to the given PF is $\phi = \arccos(PF) \cong \pm\pi/6$. The frequency spectra of the output currents [see Figs. 13(b) and 14(b)] showed that the THD values are 3.41% at 0.85 lagging PF, and 3.97% at 0.85 leading PF; these THDs also satisfy the IEEE-1547 requirements [40].

To validate the dynamic performance of the proposed inverter, the output power was varied from 300 to 500 W and vice versa. When the output power was changed, the output currents well tracked the reference output current under the power variation (see Fig. 15).

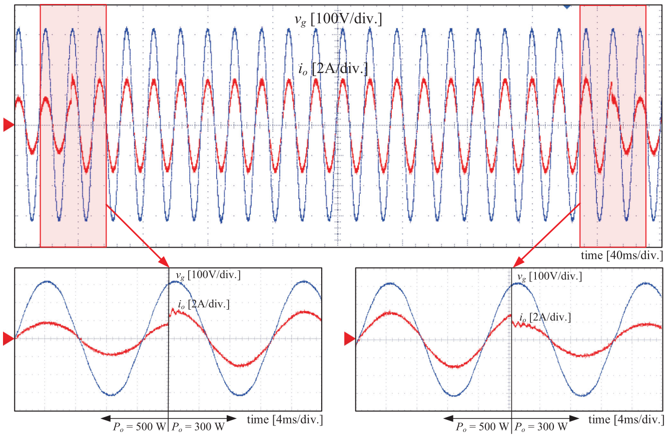

Fig. 15. Output waveforms of the grid voltage and output current when the output power is varied between 300 and 500 W.

The experimental waveforms (see Fig. 16) show that the average voltage across C_1 depended on the average input voltage, whereas the average voltage across C_2 depended upon the average grid voltage. The inverter operates in CCM during the grid period, so the currents of L_1 and L_2 did not go to zero.

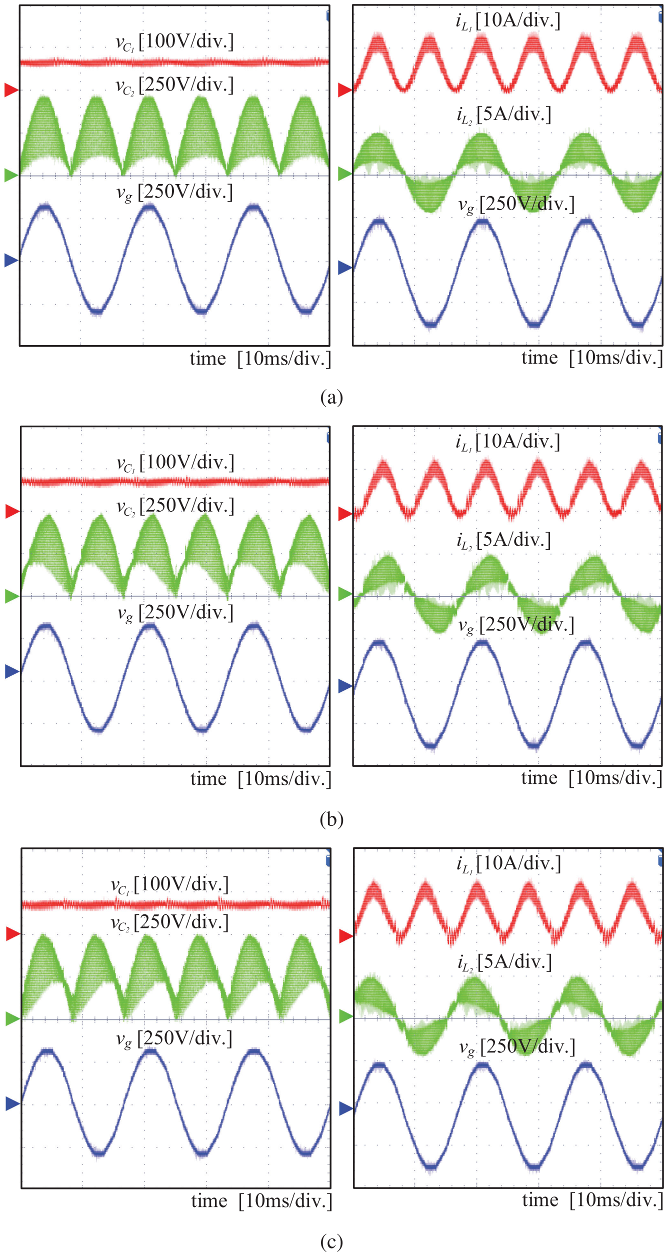

Fig. 16. Experimental waveforms of v_{C_1}, v_{C_2}, v_g, i_{L_1}, and i_{L_2}. (a) Unity power factor. (b) 0.85 lagging power factor. (c) 0.85 leading power factor.

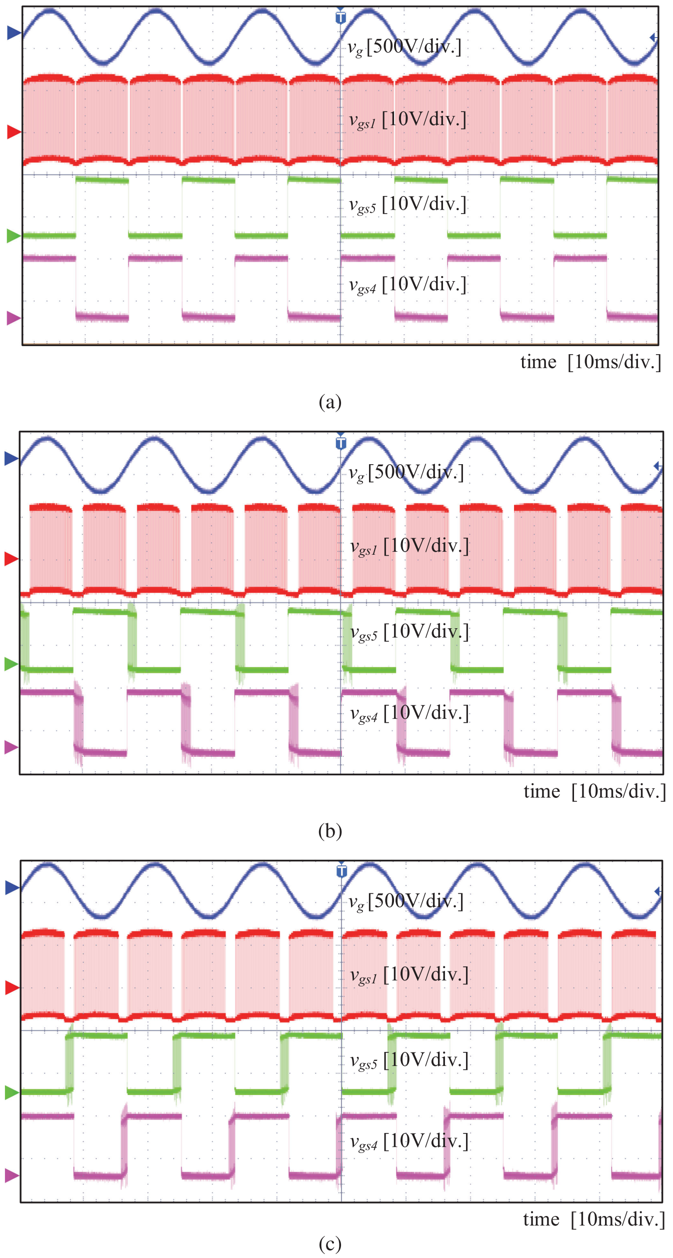

Fig. 17. Gate drive signals v_g, v_{gs1}, v_{gs4}, and v_{gs5}. (a) Unity power factor. (b) 0.85 lagging power factor. (c) 0.85 leading power factor.

The experimental gate drive signals (see Fig. 17) for S_1, S_4, and S_5 of the bridgeless Cuk-derived inverter were fully matched with the modulation scheme as in Section III. When the inverter operates at unity power factor, S_1 switches at high frequency; the body diode of S_4 conducts in a complementary way to S_1 when $v_g > 0$, and the body diode of S_5 conducts similarly to S_4 when $v_g < 0$. When the inverter operates at nonunity power factor, the operations of all the switches are the same in forward power flow but different in reverse power flow; one of S_4 or S_5 switches at high frequency of 40 kHz for the reactive-power injection [see Fig. 17(b) and (c)]. To increase the power conversion efficiency of the bridgeless Cuk-derived inverter, the inverter can operate with SR as in Section III. When the bridgeless Cuk-derived inverter operates under SR, S_4 or S_5 is selected depending upon the polarity of the grid voltage and turned ON complementarily to S_1 (see Fig. 18).

Fig. 19 shows the configuration of the reference output current generation for the MPP tracking (MPPT); the rotating reference frame is synchronized with the grid voltage v_g; the d-axis component i_{o_d} of i_o is equal to the amplitude of the output current reference obtained from the MPPT controller. The q-axis component i_{o_q} of i_o is calculated by the reference reactive power $Q_{\mathrm{o\_ref}}$; an incremental conductance method is used to compute the MPP [41]. To show the MPPT performance of the proposed inverter, a PV simulator (AMETEK) was used to emulate the dynamic behavior of the PV panel; an additional

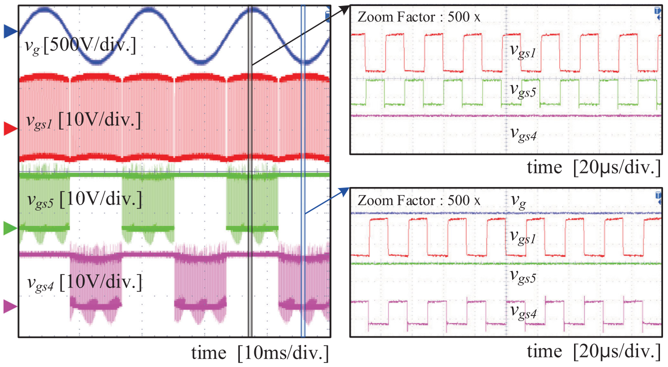

Fig. 18. Gate drive signals v_{gs1}, v_{gs2}, v_{gs3}, and v_{gs4} with the SR operation (unity power factor).

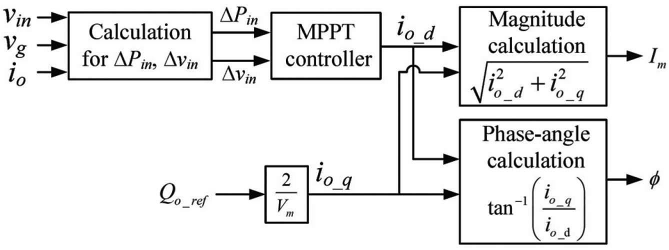

Fig. 19. Configuration of reference output current generation with MPPT.

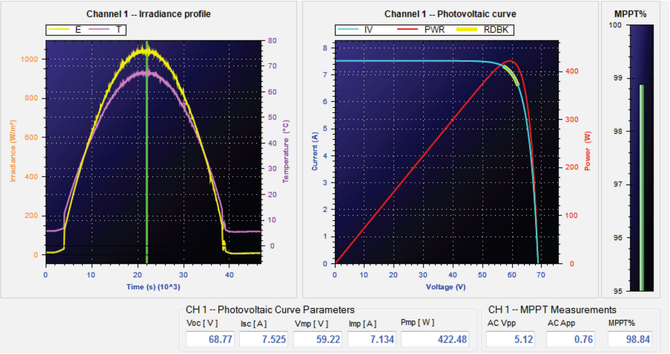

CH 1 -- Photovoltaic Curve Parameters

Voc [V]	Isc [A]	Vmp [V]	Imp [A]	Pmp [W]
68.77	7.525	59.22	7.134	422.48

CH 1 -- MPPT Measurements

AC Vpp	AC App	MPPT%
5.12	0.76	98.84

Fig. 20. Irradiance profile, PV curve, and MPPT efficiency provided by the PV simulator.

input capacitor ($C_{\text{in}} = 2$ mF) was used at the input side of the inverter. The proposed inverter well tracked the MPP, and the maximum efficiency of the MPPT was measured at 98.84% (see Fig. 20).

The efficiency (see Fig. 21) of the bridgeless Cuk-derived inverter was measured within a range of load conditions and with and without the SR operation by using a digital power meter (Yokogawa WT330). Without the SR operation, the measured maximum efficiency was 95.5%, and the California Energy Commission's (CEC) weighted efficiency was 95.1%. With the SR operation, the maximum efficiency was 96.6%, and the CEC efficiency was 95.8%. Referring to [43] and [44], the power loss distribution was also analyzed (see Fig. 22). The SR operation significantly reduces the diode loss, so the power conversion efficiency of the bridgeless Cuk-derived inverter increases.

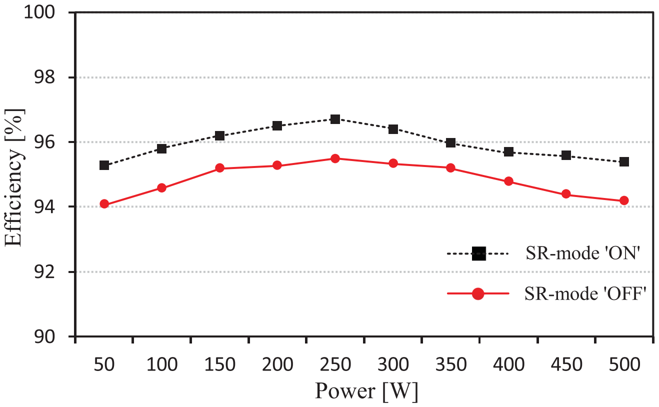

Fig. 21. Comparison of the measured efficiencies with and without the SR operation.

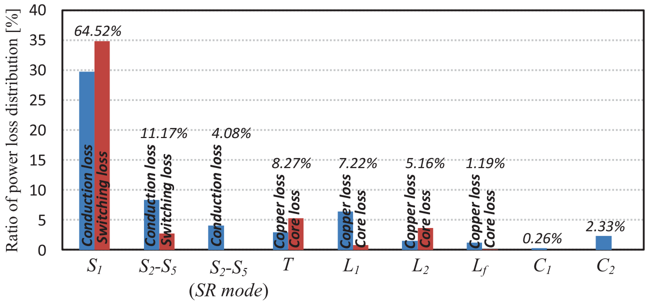

Fig. 22. Power loss distribution with and without the SR operation.

To emphasize the merits of the proposed inverter, it was compared (see Table V) with the existing solutions for the reactive-power supply in single-phase MICs. A bipolar PWM scheme in the inverters has excellent reactive-power capability in the entire grid period, but it causes high switching loss and high current ripple. Unipolar-based PWM techniques [9], [10] can also make H-bridge based inverters inject reactive power to the utility grid, while satisfying international standards, but the reactive-power-injection capability of these techniques is limited due to insufficient magnetizing force [9]. Moreover, H-bridge based inverters require an additional boost converter stage, which increases their development cost and decreases power conversion efficiency. A proposed method [24] for reactive-power supply in unfolding-type flyback inverters requires an additional decoupling circuit that increases hardware development cost. The reference waveform modification scheme [25] has been presented for the reactive-power supply by using an unfolding-type inverter without having to use any additional circuit, but the output current has quite high THD due to the different shape of the reference current. The low cost and good reactive-power capability of the proposed inverter make it an effective solution for single-phase MICs.

Two-stage inverter and Cuk-topology-based inverters are also compared in terms of current stress/voltage stress of the switches, efficiency, size/value of passive components, and control complexity (see Table VI). Here, a two-stage inverter

TABLE V
COMPARISON OF METHODS FOR REACTIVE-POWER SUPPLY IN SINGLE-PHASE MICs

	Two-stage power conversion			Unfolding-type conversion		Single power conversion
Ref.	[8]	[9]	[10]	[24]	[25]	This paper
Structure	Full-bridge inverter (BP)	H5 inverter (UP & BP)	H6 inverter (UP)	Unfolding circuit + Flyback converter + Decoupling circuit	Unfolding inverter (No boost)	Bridgeless Cuk inverter
	(+ Step-up dc-dc converter needed for MICs)					
DC input voltage	400 V	380 V	380 V	30 V	380 V	60 V
AC output voltage	230 V_{rms}	220 V_{rms}	220 V_{rms}	120 V_{rms}	120 V_{rms}	220 V_{rms}
THD min.	-	-	3.7 %	4 %	16.7 %	3.34 %
Efficiency max.	$97.6^{1)}$ %	$96.4^{1)}$ %	$97.9^{1)}$ %	-	-	96.6 %
Reactive power Capability	Full range	PF $\geq$ 0.9	PF $\geq$ 0.95	PF $\geq$ 0.95	PF $\geq$ 0.95	PF $\geq$ 0.85

$^{1)}$Power conversion efficiency of the inverter only.

TABLE VI
COMPARISON OF TWO-STAGE INVERTER AND CUK-TOPOLOGY-BASED INVERTERS IN TERMS OF HARDWARE IMPLEMENTATION AND PERFORMANCE

		Two-stage inverter	Cuk topology based inverters		
		Boost converter + H-bridge inverter	Unfolding-type Cuk inverter	Differential-mode Cuk inverter$^{2)}$	Bridgeless Cuk-derived inverter
Ref.		[42]	[21]	[28]	This paper
Size/value of components	L	$L_1 = 400\ \mu$H $L_2 = 3$ mH $L_f = 200\ \mu$H	$L_1 = 360\ \mu$H $L_2 = 680\ \mu$H $L_f = 210\ \mu$H	$L_1 = L_3 = 50\ \mu$H $L_2 = L_4 = 100\ \mu$H $L_f = 200\ \mu$H	$L_1 = 360\ \mu$H $L_2 = 1.1$ mH $L_1 = 170\ \mu$H
	C	$C_{dc} = 400\ \mu$F $C_o = 1\ \mu$F	$C_1 = 4.4\ \mu$F $C_2 = 100$ nF $C_3 = 100$ nF	$C_1 = C_4 = 5.8\ \mu$F $C_2 = C_5 = 1.5\ \mu$F $C_3 = C_6 = 4.4\ \mu$F	$C_1 = 8.8\ \mu$F $C_2 = 200$ nF $C_3 = 470$ nF
	n	-	1:2.82	1:2	1:3.1
Adopted controller		PI controller	RC with phase-lead compensation	Multiple resonant controller	RC with phase-lead compensation
Switching frequency f_s		S_{1-5}: 10 kHz	S_1 & D_1: 40 kHz S_{2-5}: 60 Hz	S_{1-2} (or S_{3-4}) : 100 kHz	S_1 & S_4 (or S_5): 40 kHz S_{2-3}: 60 Hz
Voltage stress$^{1)}$ of switch		S_1: 0.3 p.u S_{2-5}: 1.2 p.u	S_1: 0.5 p.u, D_1: 1.6 p.u $S_{3,4}$(or $S_{2,5}$): 1.0 p.u	S_1(or S_3): 0.5 p.u S_2(or S_4): 1.6 p.u S_3(or S_1): 0.2 p.u	S_1: 0.5 p.u S_2(or S_3): 1.0 p.u S_5(or S_4): 1.6 p.u
Current stress$^{1)}$ of switch		S_1: 10.3 p.u S_{2-5}: 1.0 p.u	S_1: 8.3 p.u, D_1: 2.6 p.u $S_{2,5}$(or $S_{3,4}$): 1,0 p.u	S_1(or S_3): 8.3 p.u S_2(or S_4): 2.6 p.u S_4(or S_2): 1.0 p.u	S_1: 8.3 p.u S_3(or S_2): 1.6 p.u S_4(or S_5): 1.0 p.u S_5(or S_4): 2.6 p.u
Efficiency		93.2 %	94.7 %	94.1 %	95.1 %
THD		4.62 %	3.71 %	4.12 %	3.06 %
Leakage current		$<$ 120 mA	$\cong$ 0 A	$\cong$ 0 A	$\cong$ 0 A

$^{1)}$Benchmark value - switch voltage and current stresses, $v_g = 1.0$ p.u., $i_o = 1.0$ p.u. at the instantaneous peak power with full load $P_o = 500$ W and the dc-link voltage $= 380$ V.
$^{2)}$Implemented in discontinuous modulation scheme [28].

consists of boost converter and H-bridge inverter with bipolar modulation. Using the PSIM software, simulations were conducted for the two-stage inverter [42] and Cuk-derived inverters [21], [28] under the same operating condition ($P_o = 500$ W, $v_{\text{in}} = 60$ V, $v_g = 220$ V/60 Hz). Two-stage power conversion results in low power conversion efficiency. Since it does not have a transformer, it would suffer from leakage current problem. Also, the size of the output inductor is relatively large. The unfolding-type Cuk inverter achieved high efficiency with reduced number of power components. At unfolding stage, switching loss is almost zero. Since it has a transformer, it would not suffer from leakage current problem. The size of the output inductor is small enough. However, it cannot generate reactive current due to the unfolding stage operation. On the other hand, the differential-mode inverter can generate reactive current and inject it into the grid. One of the two bidirectional Cuk converters operates when grid voltage is positive or negative. It requires a reduced number of active components, but it also requires many passive-power components. The proposed bridgeless Cuk-derived inverter features a reduced number of power components, high efficiency, and reactive-power-transfer capability.

VI. CONCLUSION

This paper has presented a bridgeless Cuk-derived single power conversion inverter. The inverter features reactive-power capability with fewer components and, thus, lower cost than that of the existing Cuk-based inverters for MIC uses. To reduce the number of active-power components, the secondary-side diode into the secondary-side switches was integrated. We developed the modulation technique for the bridgeless Cuk-derived inverter to inject the active/reactive power to the utility grid. To achieve accurate tracking of the output current, we used an RC coupled with the linear feedback controller and the feedforward controller. We also propose the design guidelines for the proposed converter. To confirm its validity, a 500-VA prototype inverter was built and tested. The proposed bridgeless Cuk-derived inverter operating in SR mode achieved the maximum efficiency of 96.6% and a power factor of 0.85 under both leading and lagging conditions.

REFERENCES

[1] M. Mirjafari, S. Harb, and R. Balog, “Multiobjective optimization and topology selection for a module-integrated inverter,” *IEEE Trans. Power Electron.*, vol. 30, no. 8, pp. 4219–4231, Aug. 2015.

[2] “Solar micro inverter—Global market outlook (2017–2023),” Statistics Market Research Consulting Pvt. Ltd., Gaithersburg, MD, USA, Rep., Jun. 2013.

[3] “Generators connected to the LV distribution network-technical requirements for the connection to and parallel operation with low-voltage distribution networks,” Verband der Elektrotechnik, Frankfurt am Main, Germany, Tech. Rep. VDE-AR-N 4105, Aug. 2011.

[4] T. LaBella, W. Yu, J. S. Lai, M. Senesky, and D. Anderson, “A bidirectional-switch-based wide-input range high-efficiency isolated resonant converter for photovoltaic applications,” *IEEE Trans. Power Electron.*, vol. 29, no. 7, pp. 3473–3484, Jul. 2014.

[5] S. Poshtkouhi and O. Trescases, “Flyback mode for improved low-power efficiency in the dual-active-bridge converter for bidirectional PV microinverters with integrated storage,” *IEEE Trans. Ind. Appl.*, vol. 51, no. 4, pp. 3316–3324, Jul./Aug. 2015.

[6] W. Cha, Y. Cho, J. Kwon, and B. Kwon, “Highly efficient microinverter with soft-switching step-up converter and single-switch-modulation inverter,” *IEEE Trans. Ind. Electron.*, vol. 62, no. 6, pp. 3516–3523, Jun. 2015.

[7] C. Lam, W. Choi, M. Wong, and Y. Han, “Adaptive DC-link voltage-controlled hybrid active power filters for reactive power compensation,” *IEEE Trans. Power Electron.*, vol. 27, no. 4, pp. 1758–1772, Apr. 2012.

[8] Y. Yang, F. Blaabjerg, and H. Wang, “Low-voltage ride-through of single-phase transformerless photovoltaic inverters,” *IEEE Trans. Ind. Appl.*, vol. 50, no. 3, pp. 1942–1952, May/Jun. 2014.

[9] T. Wu, C. Kuo, K. Sun, and H. Hsieh, “Combined unipolar and bipolar PWM for current distortion improvement during power compensation,” *IEEE Trans. Power Electron.*, vol. 29, no. 4, pp. 1702–1709, Apr. 2014.

[10] B. Liu, M. Su, J. Yang, D. Song, D. He, and S. Song, “Combined reactive power injection modulation and grid current distortion improvement approach for H6 transformer-less photovoltaic inverter,” *IEEE Trans. Energy Convers.*, vol. 32, no. 4, pp. 1456–1467, Dec. 2017.

[11] J. Wang *et al.*, “An improved hybrid modulation method for the single-phase H6 inverter with reactive power compensation,” *IEEE Trans. Power Electron.*, vol. 33, no. 9, pp. 7674–7683, Sep. 2018.

[12] T. Freddy, J. Lee, H. Moon, K. Lee, and N. Rahim, “Modulation technique for single-phase transformerless photovoltaic inverters with reactive power capability,” *IEEE Trans. Ind. Electron.*, vol. 64, no. 9, pp. 6989–6999, Sep. 2017.

[13] Z. Zhang, X.-F. He, and Y.-F. Liu, “An optimal control method for photovoltaic grid-tied-interleaved flyback microinverters to achieve high efficiency in wide load range,” *IEEE Trans. Power Electron.*, vol. 28, no. 11, pp. 5074–5087, Nov. 2013.

[14] N. Sukesh, M. Pahlevaninezhad, and P. K. Jain, “Analysis and implementation of a single-stage flyback PV microinverter with soft switching,” *IEEE Trans. Ind. Electron.*, vol. 61, no. 4, pp. 1819–1833, Apr. 2014.

[15] M. Rezaei, K. Lee, and A. Huang, “A high-efficiency flyback micro-inverter with a new adaptive snubber for photovoltaic applications,” *IEEE Trans. Power Electron.*, vol. 31, no. 1, pp. 318–327, Jan. 2016.

[16] M. A. Rezaei, K. J. Lee, and A. Q. Huang, “A high-efficiency flyback micro-inverter with a new adaptive snubber for photovoltaic applications,” *IEEE Trans. Ind. Electron.*, vol. 31, no. 1, pp. 318–327, Jan. 2016.

[17] K. Kim, S. Lee, W. Cha, J. Kwon, and B. Kwon, “Bidirectional single power-conversion DC–AC converter with noncomplementary active-clamp circuits,” *IEEE Trans. Ind. Electron.*, vol. 63, no. 8, pp. 4860–4867, Aug. 2016.

[18] T. Thang, N. Thao, J. Jang, and J. Park, “Analysis and design of grid-connected photovoltaic systems with multiple-integrated converters and a pseudo-DC-link inverter,” *IEEE Trans. Ind. Electron.*, vol. 61, no. 7, pp. 3377–3386, Jul. 2014.

[19] S. Lee, W. Cha, B. Kwon, and M. Kim, “Discrete-time repetitive control of flyback CCM inverter for PV power applications,” *IEEE Trans. Ind. Electron.*, vol. 63, no. 2, pp. 976–984, Feb. 2016.

[20] H. Kim, J. Lee, J. Lai, and M. Kim, “Iterative learning controller with multiple phase-lead compensation for dual-mode flyback inverter,” *IEEE Trans. Power Electron.*, vol. 32, no. 8, pp. 6468–6480, Sep. 2016.

[21] B. Han, J. S. Lee, and M. Kim, “Repetitive controller with phase-lead compensation for Cuk CCM inverter,” *IEEE Trans. Ind. Electron.*, vol. 65, no. 3, pp. 2356–2367, Mar. 2018.

[22] B. Han, J.-S. Lai, and M. Kim, “Dynamic modeling and controller design of dual-mode Cuk inverter in grid-connected PV/TE applications” *IEEE Trans. Power Electron.*, vol. 33, no. 10, pp. 8887–8904, Oct. 2018.

[23] S. Cuk and R. D. Middlebrook, “Advances in switched-mode power conversion part II,” *IEEE Trans. Ind. Electron.*, vol. IE-30, no. 1, pp. 19–29, Feb. 1983.

[24] E. Fonkwe, J. Kirtley, and J. Elizondo, “Flyback micro-inverter with reactive power support capability,” in *Proc. IEEE 17th Workshop Control Model. Power Electron.*, 2016, pp. 1–8.

[25] D. Li, C. Ngai, L. Liu, and G. Escobar, “Reactive power control for single-phase grid-tie inverters using quasi-sinusoidal waveform,” *IEEE Trans. Sustain. Energy*, vol. 9, no. 1, pp. 3–11, Jan. 2018.

[26] T. Isobe, D. Shiojima, K. Kato, Y. R. R. Hernandez, and R. Shimada, “Full-bridge reactive power compensator with minimized-equipped capacitor and its application to static var compensator,” *IEEE Trans. Power Electron.*, vol. 31, no. 1, pp. 224–234, Jan. 2016.

[27] C. Lam, W. Choi, M. Wong, and Y. Han, “Adaptive DC-link voltage-controlled hybrid active power filters for reactive power compensation,” *IEEE Trans. Power Electron.*, vol. 27, no. 4, pp. 1758–1772, Apr. 2012.

[28] S. Mehrnami and S. K. Mazumder, “Discontinuous modulation scheme for a differential-mode Cuk Inverter,” *IEEE Trans. Power Electron.*, vol. 30, no. 3, pp. 1242–1254, Mar. 2015.

[29] H. Soni, S. K. Mazumder, A. Gupta, D. Chatterjee, and A. Kulkarni, “Control of isolated differential-mode single-and three-phase Cuk inverters at module level,” *IEEE Trans. Power Electron.*, vol. 33, no. 10, pp. 8872–8886, Oct. 2018.

[30] P. T. Krein and R. M. Bass, “Autonomous control technique for high performance switches,” *IEEE Trans. Ind. Electron.*, vol. 39, no. 3, pp. 215–222, Jun. 1992.

[31] V. Yousefzadeh and D. Maksimovic, “Sensorless optimization of dead times in DC–DC converters with synchronous rectifiers,” *IEEE Trans. Power Electron.*, vol. 21, no. 3, pp. 994–1002, Jul. 2006.

[32] J. Abu-Qahouq, H. Mao, H. Al-Atrash, and I. Batarseh, “Maximum efficiency point tracking (MEPT) method and dead time control,” *IEEE Trans. Power Electron.*, vol. 21, no. 5, pp. 1273–1281, Sep. 2006.

[33] A. Peterchev and S. Sanders, “Digital multi mode buck converter control with loss-minimizing synchronous rectifier adaptation,” *IEEE Trans. Power Electron.*, vol. 21, no. 6, pp. 1588–1599, Nov. 2006.

[34] M. Zhang, M. Jovanovic, and F. Lee, “Design considerations and performance evaluations of synchronous rectification in flyback converters,” *IEEE Trans. Power Electron.*, vol. 13, no. 3, pp. 538–546, May 1998.

[35] Z. Ouyang and M. Andersen, “Overview of planar magnetic technology—Fundamental properties,” *IEEE Trans. Power Electron.*, vol. 29, no. 9, pp. 4888–4900, Sep. 2014.
[36] C. Pan, M. Cheng, and C. Lai, “A novel integrated DC/AC converter with high voltage gain capability for distributed energy resource systems,” *IEEE Trans. Power Electron.*, vol. 27, no. 5, pp. 2385–2395, May 2012.
[37] V. Bist and B. Singh, “A unity power factor bridgeless isolated Cuk converter-fed brushless DC motor drive,” *IEEE Trans. Ind. Electron.*, vol. 62, no. 7, pp. 4118–4129, Jul. 2015.
[38] A. Reznik, M. Simoes, A. Al-durra, and S. Muyeen, “LCL filter design and performance analysis for grid-interconnected systems,” *IEEE Trans. Ind. Appl.*, vol. 50, no. 2, pp. 1225–1232, Mar./Apr. 2014.
[39] “Software phase locked loop design using C2000TM microcontroller for single phase grid connected inverter,” Texas Instruments Inc., Dallas, TX, USA, Appl. Rep., Jun. 2013.
[40] *IEEE Standard for Interconnection and Interoperability of Distributed Energy Resources With Associated Electric Power Systems Interfaces*,” *IEEE Standard 1547–2018 (Revision of IEEE Standard 1547–2003)*, Apr. 2018.
[41] J. Kwon, K. Nam, and B. Kwon, “Photovoltaic power conditioning system with line connection,” *IEEE Trans. Ind. Electron.*, vol. 53, no. 4, pp. 1048–1054, Aug. 2006.
[42] H. Liu, P. Loh, X. Wang, Y. Yang, W. Wang, and D. Xu, “Droop control with improved disturbance adaption for a PV system with two power conversion stages,” *IEEE Trans. Ind. Electron.*, vol. 63, no. 10, pp. 6073–6085, Oct. 2016.
[43] R. Yu, B. Pong, B. Ling, and J. Lam, “Two-stage optimization method for efficient power converter design including light load operation,” *IEEE Trans. Power Electron.*, vol. 27, no. 3, pp. 1327–1337, Mar. 2012.
[44] C. Larouci, M. Boukhnifer, and A. Chaibet, “Design of power converters by optimization under multiphysic constraints: Application to a two-time-scale AC/DC–DC converter,” *IEEE Trans. Ind. Electron.*, vol. 57, no. 11, pp. 3746–3753, Nov. 2010.

Byeongcheol Han (S’15–M’18) was born in Busan, South Korea, in 1986. He received the B.S degree in electrical engineering from Pusan National University, Busan, South Korea, in 2012, and the Ph.D. degree in creative IT engineering (CiTE) from Pohang University of Science and Technology (POSTECH), Pohang, South Korea, in 2018.

In 2018, he was a Postdoctoral Researcher in CiTE with POSTECH. Since 2018, he has been a Postdoctoral Associate with the Future Energy Electronics Center, Virginia Tech, Blacksburg, VA, USA. His research interests include nonlinear systems and control, grid-connected inverters, energy storage systems, and controller design for power conversion systems.

Jih-Sheng (Jason) Lai (S’85–M’89–SM’93–F’07–LF’19) received the M.S. and Ph.D. degrees in electrical engineering from the University of Tennessee, Knoxville, TN, USA, in 1985 and 1989, respectively.

In 1989, he joined the Electric Power Research Institute (EPRI) Power Electronics Applications Center, where he managed EPRI-sponsored power electronics research projects. In 1993, he joined the Oak Ridge National Laboratory as a Power Electronics Lead Scientist, where he initiated a high power electronics program and developed several novel high power converters including multilevel converters and soft-switching inverters. In 1996, he joined Virginia Polytechnic Institute and State University, Blacksburg, VA, USA, where he is currently the James S. Tucker Professor with the Department of Electrical and Computer Engineering and Director of Future Energy Electronics Center. He has authored or coauthored more than 450 refereed technical papers, a book chapter, two books, and invented 27 patents. His main research areas are in high efficiency power electronics conversion for high power and energy applications.

Prof. Lai was the recipient of the Technical Achievement Award in Lockheed Martin Award Night, two Journal Paper Awards, and 12 Best Paper Awards from IEEE sponsored conferences. He was also the recipient of the 2016 IEEE IAS Gerald Kliman Innovator Award. He led the student teams to win the top three finalist positions in the Google Little Box Challenge in 2016, the Grand Prize Award from the International Future Energy Challenge in 2011, and the Grand Prize Award from Texas Instruments Engibous Analog Design Competition in 2009. He is the one of the Founding Chairs of the 2001 IEEE IFEC and 2016 IEEE ACEPT, and he is also one of the General Chairs of the IEEE COMPEL-2000, the IEEE APEC 2005, the IEEE SPEC-2018, and the IEEE IFEEC-2019 conferences.

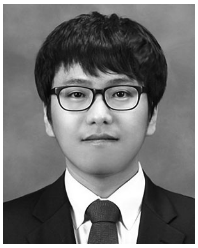

Minsung Kim (M’14) was born in Ulsan, South Korea, in 1986. He received the B.S. degree in electrical engineering, in 2008, and the Ph.D. degree in electrical engineering, in 2013, both from Pohang University of Science and Technology (POSTECH), Pohang, South Korea.

Since 2013, he has been with the Department of Creative IT Engineering and Future IT Research Laboratory, POSTECH, Pohang, Korea, where he was a Research Assistant Professor. In 2016, he was a Research Scholar with Future Energy Electronics Center, Virginia Tech. In 2017, he was an Academic Visitor with the Control and Power System Group, Imperial College London. Since 2018, he has been with the Division of Electronics and Electrical Engineering, Dongguk University, Seoul, South Korea, where he is currently an Assistant Professor. His current research interests include highly efficient power conversion circuit design, intelligent controller design for industrial electronics, and renewable energy and energy storage systems.